# 12 Modern Characterization Techniques for Crude Oils, Their Emulsions, and Functionalized Surfaces

*Johan Sjöblom, Gisle Øye, Wilhelm R. Glomm, Andreas Hannisdal, Magne Knag, Øystein Brandal, Marit-Helen Ese, Pål V. Hemmingsen, Trond E. Havre, Hans-Jörg Oschmann, and Harald Kallevik*

**CONTENTS**

## 12.1 INTRODUCTION

Crude oil exploitation offshore has advanced to the point, at least on the Norwegian Continental Shelf, where the era of large fields with a high quantity and quality is over. Since the possibility of finding highly productive formations is small the corresponding strategy is focused on an improved exploitation of the existing large fields and to tie in, in an efficient way, small fields. The most important thing when focusing on existing large fields is to increase the recovery rate. This, however, can be connected with typical flow assurance problems. At older fields the co-production of water is in most cases substantial. It is well known that many wells co-produce water to an extent of 50 to 70%. This production profile will cause problems with high water volumes in the separator and emulsions close to the inversion point.

To tie in small fields with larger production streams means that the fluids that are to be mixed must be compatible. If one encounters precipitation of organic matter (for instance asphaltenes) the whole production line and the regularity will be endangered.

In parallel with these efforts the trend to build up a sub-sea processing network will emerge. Also in this case the nature of the fluids will be decisive for the design and dimensions of the process unit. Since this unit will function on a sea depth of 300 to 400 m (in the future about 1000 m) it is obvious that maintenance operations are very costly and should be rare.

A central question when solving the design of the process unit is the nature of the fluids that are to be processed. Hence fluid characterization will be a key technology for success in the future offshore processing.

In this chapter we present modern instrumentation for such a fluid characterization. We cover the basic theory behind the measurements together with recent examples. We have also included some examples on characterization of functionalized solid surfaces.

At the Ugelstad laboratory, as at many other modern laboratories, we aim at doing good analytical chemical characterization of components in the crude oil as well as mapping the physicochemical properties of these components.

## 12.2 ANALYTICAL CHEMICAL CHARACTERIZATION

### 12.2.1 SARA Fractionation by High Performance Liquid Chromatography

Crude oils have a complex nature and it is not possible to determine the individual molecular constituents. Compositional studies are usually done by fractionation into predefined chemical families. The SARA group type fractionation separates the crude oil into the following classes: saturates, aromatics, resins, and asphaltenes. The definition of the SARA fractions is well accepted and will not be presented in detail here. Speight [1] gives a thorough introduction to the chemistry and structure of crude oil. In short, saturates are defined as the saturated hydrocarbons ranging from straight-chain paraffins to cycloparaffins (napthenes) while the aromatic fraction includes hydrocarbons containing one or more aromatic nuclei which may be substituted with napthenes or paraffins. Asphaltenes are defined as the solubility class of crude oils that precipitate in the presence of aliphatic solvents (here n-hexane or n-pentane) while the resin fraction is defined as the fraction soluble in light alkanes but insoluble in liquid propane [1]. Asphaltenes and resins are known as large, polar, polynuclear molecules consisting of condensed aromatic ring systems and heteroatoms like sulfur, nitrogen, and oxygen. Asphaltenes and resins have gained increased interest with the knowledge of the large effect of these constituents in particular on the overall performance of heavy crude oils.

Although the SARA fractionation method is just a rough sorting of the crude oil constituents, it provides an important classification of crude oils. As will be seen from other examples of applications in this chapter, SARA characteristics are frequently used when discussing different crude oil properties. The SARA fractionation method has found great utility in combination with high-performance liquid chromatography (HPLC) [2–6]. HPLC is an analytical technique for the separation and determination of organic and inorganic solutes in any sample, especially biological, pharmaceutical, food, environmental, and industrial. In a normal-phase liquid chromatographic process a nonpolar mobile phase permeates through a porous solid stationary phase (polar) usually in the form of small uniform particles, packed into a cylindrical column. The sample is injected into the mobile phase, travels through the column, and is retained by the stationary phase mainly depending on polarity. Adsorption interactions between sample components, the mobile phase, and the stationary phase can be manipulated by the choice of mobile and stationary phases and flow conditions.

As an example of the SARA fractionation method we will discuss the procedure from a study by Hannisdal and co-workers [7]. The ability of vibrational spectroscopy to predict SARA components in heavy and particle rich crude oil will be discussed in the following section.

In this study, 20 crude oil samples at ambient temperature and pressure were received from exploration sites on the Norwegian Continental Shelf and sites located in Brazil, France, the South China Sea, the Atlantic Ocean, and the Gulf of Mexico. These oils were quantitatively fractionated into saturates, aromatics, resins, and asphaltenes (SARA) by asphaltene precipitation in n-hexane and preparative HPLC. Here, the focus will be on the HPLC procedure.

The HPLC system used in this study was built up from the modules shown schematically in Figure 12.1. Two columns were used: one 21.2 × 250 mm column packed with unbonded silica 15 μm and one 21.2 × 50 mm amino (10 μm) column. Dichloromethane (99.8%) and n-hexane (95%) were used as mobile phases. Generally, preparative separations of organic samples favor the use of unmodified silica as column packing material [8]. However, experiments on the preparative silica column showed that dichloromethane did not have the necessary solvent strength to elute the most polar components in heavy crude oils. These resins were irreversibly adsorbed onto the silica packing material. Instead an amino column, weaker in column strength, was used for this study in a multidimensional column setup shown in Figure 12.2. The two

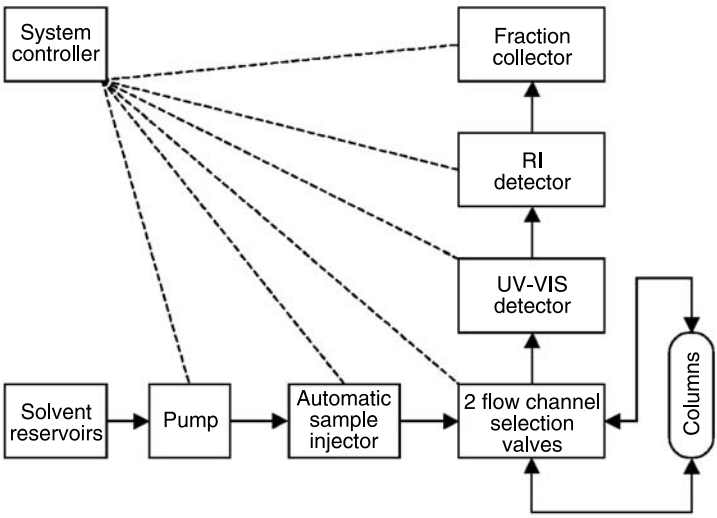


**FIGURE 12.1** Schematic representation of the HPLC system with main modules.

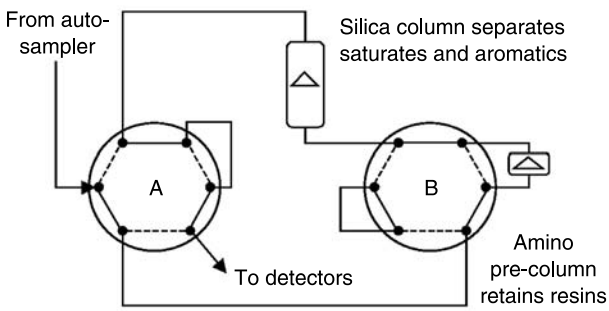


**FIGURE 12.2** Scheme of the flow channel selection valves. Valve A controls the flow direction through columns (normal/backflush) while valve B includes or excludes the amino pre-column.

selection valves shown in the figure allow an individual reloading of the two columns. Valve A controls the flow direction through columns (normal/backflush) while valve B includes or excludes the pre-column. The new setup reduced the time of analysis from 70 to 26 min.

A sample of 5 ml asphaltene-free crude oil in n-hexane (corresponding to 0.6 g crude oil) was injected into the 20 ml/min flow (isocratic) of filtrated and degassed n-hexane. Crude oil components travel through the columns and are retained mainly depending on polarity. Saturates, having no retention on the columns, are collected from RI signals (3 to 5 min). After 15 min, all aromatics have left the amino pre-column but some condensed polycyclic aromatic ring systems are not yet eluted from the silica column. These are collected from the preparative column by dichloromethane backflush (<23 min) while the resin fraction is desorbed from the amino pre-column by dichloromethane backflush, 23 to 26 min after sample injection. This procedure provides the chromatogram in Figure 12.3 where the three fractions are well resolved. The SAR

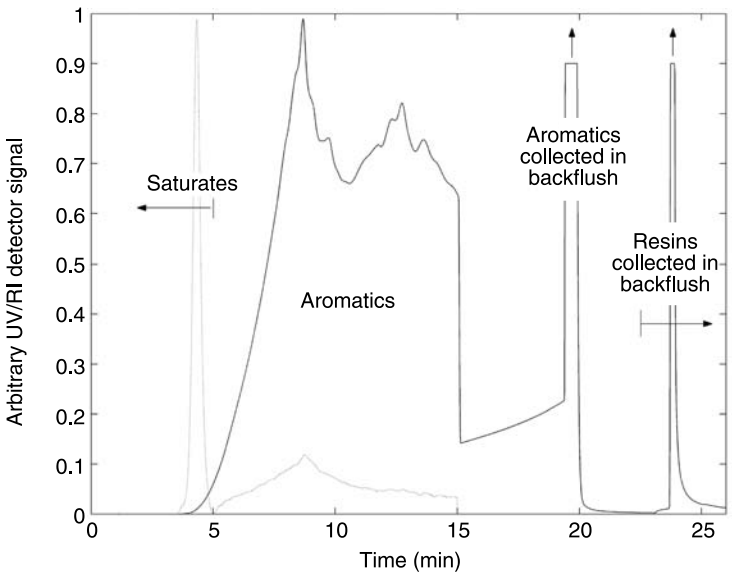


**FIGURE 12.3** Typical chromatogram from preparative HPLC analysis. The solid line represents the RI signal while the broken line represents the UV chromatogram at 254 nm. Peaks are cut for better visualization.

weight fractions are determined gravimetrically after controlled evaporation of solvents in an $N_2$ atmosphere.

This example shows how SARA values are determined using a procedure for asphaltene preprecipitation followed by automated preparative high performance liquid chromatography. The discussed HPLC method had a sample capacity corresponding to 0.6 g of heavy crude oil. Since the determination of the SARA components is done gravimetrically, larger sample capacity will improve the accuracy of the procedure significantly. Moreover, the large sample capacity allows further characterization of the individual SARA fractions.

### 12.2.2 SARA Fractionation by Automated TLC-FID

In this section we will describe how the SARA fractions can be separated and quantified by means of thin layer chromatography (TLC) in combination with an automated flame ionization detector (FID). This method is of great benefit when there is a need to run a larger number of samples on a routine basis.

The sample to be analyzed is diluted and spotted on quartz rods that are coated with sintered silica particles. The four SARA fractions are then separated to various positions on the rods. This is done by successively emersing the rods into three development tanks containing solvents of various polarity; nonpolar solvent for saturates and increasing polarity for the aromatics and resin fractions. In the first tank n-heptane is eluated almost to the top of the rod and thereby separating the saturates from the rest of the sample. The rods are then taken out and dried before being placed in the second tank containing 80% toluene and 20% n-heptane. Here the aromatics fraction is separated as the solvent moves up the rod. The solvent is eluated to a lower height on the rod than in the first tank so that the aromatic fraction does not mix with the already separated saturate fraction. In the last development tank 95% dichloromethane and 5% methanol is used

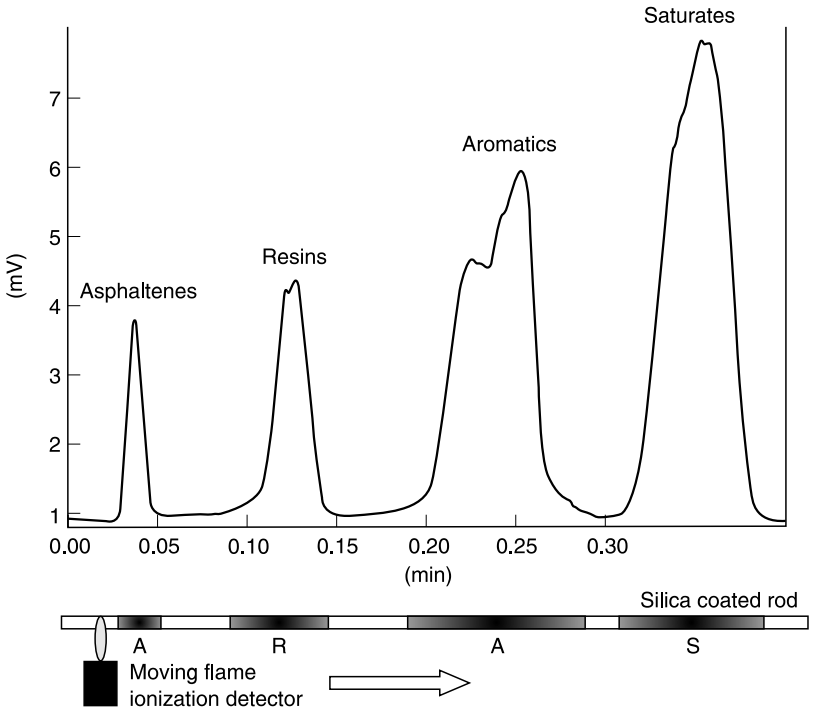


**FIGURE 12.4** After being prepared in the three development tanks, the SARA fractions can be found at various positions on the silica coated rod. The flame ionization detector moves along the rod and the resulting signal is plotted as a function of its position. The SARA fractions are quantified by integrating the corresponding peak.

to separate the resins from the asphaltenes, which will be irreversibly adsorbed to the silica rod and will stay at the same position where the sample was first spotted.

The amount of the various fractions is determined by a moving flame ionization detector (FID), which moves along the entire length of the rods. Figure 12.4 illustrates a typical chromatogram that is obtained from such analysis where the FID signal is plotted as a function of the position on the rod. The SARA fractions are quantified by integrating each peak and assuming the same response factor for all four fractions.

The SARA fraction as determined by the TLC-FID method is described in the IP 469/01 standard [9]. Given the differences in the principle for the TLC-FID method compared to the HPLC or the clay-gel absorption method [10], it is obvious that there will be some differences in the obtained results. The magnitude of the differences depends on the nature of the crude oil. Fan and Buckley [11] pointed out that volatile components will evaporate during the TLC procedure; thus underestimating the saturates and aromatics. This fact makes the TLC-FID procedure less suitable for crude oils with high amount of volatiles. Bharati and co-workers [12,13] have developed a North Sea oil based standard for the TLC-FID method. The use of this standard improves the accuracy of the obtained data, and data comparison between laboratories becomes more reliable.

The TLC-FID instrumentation is known in the industry under the name "Iatroscan." This instrument is gaining increased popularity due to the fast and easy way of performing SARA

analysis. The amount of sample needed is only 100 mg or less, which is beneficial in cases where the amount of sample is limited.

Another way of determining the SARA fractions is by means of near-infrared spectroscopy in combination with multivariate analysis. This method is described in the following section.

### 12.2.3 Near-Infrared Spectroscopy

Over the last 30 years near-infrared spectroscopy (NIR) has been increasingly used as an analytical tool, particularly by the food and agricultural industries, but also by the textiles, polymers, and petroleum industries. The increasing popularity is due to four principal advantages of the method: efficiency, simplicity, multiplicity of analysis from a single spectrum, and the nonconsumption of the samples. The rapid development of advanced and user-friendly software for multivariate analysis further enhances the usability of NIR. Optical fibers can be used to carry the light from the light source to the point of measurement and back to the light detector. This makes NIR applicable on-line in many processes.

The near-infrared region is found between the visible and middle infrared regions (MIR) of the electromagnetic spectrum. The absorption spectra in the NIR range from 780 to 2500 nm (12820 to 4000 $cm^{-1}$) consist of overtones and combinations of the fundamental molecular vibration bands, which are primarily due to stretches of hydrogen in C-H, N-H, S-H, and O-H bonds. This makes NIR an excellent choice for hydrocarbon analysis, where functional groups such as methylenic, olefinic, and aromatic C-H give rise to various C-H stretching vibrations that are mainly independent of the rest of the molecule. In addition to molecular absorption, the NIR spectra are dependent upon several physical parameters, where the most prominent is scattering from particles. As the particle size changes it causes a change in the amount of radiation scattered by the sample, and this is reflected in the NIR spectra as a shift of the baseline. For slightly lossy dielectric spheres in the Rayleigh limit ($r/\lambda \leq 0.05$, where $\lambda$ is the wavelength of incident light), the scattering and absorption processes contribute separately to the extinction coefficient. That is:

$$\sigma_{tot} = \sigma_{sc} + \sigma_{abs} \tag{12.1}$$

where $\sigma_{tot}$, $\sigma_{sc}$, and $\sigma_{abs}$ are, respectively, the total, scattering, and absorption cross-sections. The ratio of scattering to absorption scales with $r^3$, indicating the importance of particle size on the total light extinction. The relation between optical density (OD), light intensity ($I$), particle diameter ($N$), and particle cross-section ($\sigma_{tot}$) is given as:

$$\text{OD} = \log(I_0/I) = 0.434 N \sigma_{tot} \tag{12.2}$$

where $I_0$ and $I$ are the intensities of incident and transmitted light. The effect of multiple scattering is not accounted for in this equation. Details on light scattering in the near-infrared region can be found in the literature [14,15].

#### 12.2.3.1 Applications

The applications of near-infrared spectroscopy in the oil industry are numerous and much work has been done in our group within this area. Generally, these applications of NIR spectroscopy can be divided into two groups:

- For prediction of physicochemical properties
- For studies of the degree of aggregation and/or aggregation size

To give an impression of the diversity of applications, we will briefly present some examples of recent work using NIR spectroscopy.

#### 12.2.3.1.1 Prediction of SARA Values Using NIR in Combination with Multivariate Analysis

Since the SARA fractionation method presented in Section 12.2.1 is time consuming and requires expensive laboratory equipment, and some attempts have been made recently to find alternative analytical options. Aske and co-workers have shown the ability of NIR spectroscopy in combination with partial least squares (PLS) regression to predict SARA components in lighter crude oils and condensates [16]. Subsequently, Hannisdal and co-workers carried out a similar study, where the range of application was extended to particle rich and heavy crude oils [7]. Regression models were built for each SARA component from NIR data to predict the amount of SARA components. These models successfully fitted the experimental data from NIR analyzes and showed good predictive ability for the crude oil composition. This is a typical example of the ability of NIR to reflect chemical properties through vibrational characteristics as well as electronic absorption from asphaltenes.

#### 12.2.3.1.2 Prediction of Solubility Parameters

In another study recently performed in our group [17] NIR and MIR spectra were correlated to the Hildebrand [18] and Hansen solubility parameters [19–21], using multivariate data analysis. Models were built from NIR and MIR spectra of different solvents and solvent mixtures. Table 12.1 shows the results from the correlation of solubility parameters to NIR spectra. This work will be useful in order to predict solubility parameters for crude oils and asphaltenes, and ultimately asphaltene stability.

#### 12.2.3.1.3 Emulsion Stability Correlated to Physicochemical Parameters and NIR

In a study by Aske and co-workers [22], emulsion stability as measured by the critical electric field method ($E_{critical}$ presented later) was correlated to physicochemical properties and NIR spectra of 21 crude oils. Analysis of the significance of the regression coefficients of the model revealed that the NIR spectra, among some other factors, were closely correlated to the measured emulsion stability. Based on this, an attempt was made to predict emulsion stability exclusively

**TABLE 12.1**
**Results from PLS Modeling and Predictions Based on the Correlation of Solubility Parameters to Unmodified NIR Spectra**

| Quality parameters | Hildebrand (Total) | Dispersive parameter | Hydrogen bonding | Polar contribution |
|---|---|---|---|---|
| Principal components | 4 | 4 | 2 | 4 |
| Correlation validation | 0.92 | 0.88 | 0.95 | 0.95 |
| Correlation prediction | 0.92 | 0.53 | 0.91 | 0.78 |
| RMSEV ($MPa^{1/2}$) | 1.8 | 0.6 | 1.7 | 1.1 |
| RMSEP ($MPa^{1/2}$) | 2.6 | 1.1 | 3.5 | 3.8 |
| Explained *Y*-variance (%) | 87 | 81 | 90 | 89 |
| Explained *X*-variance (%) | 80 | 84 | 67 | 82 |

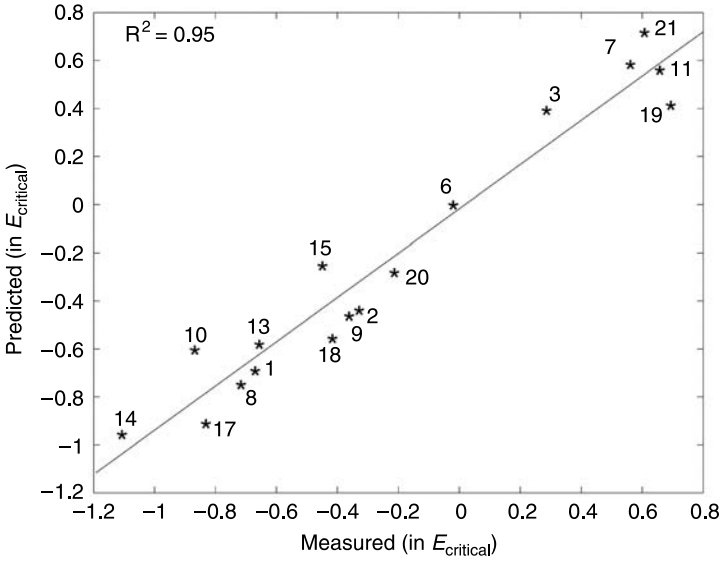


**FIGURE 12.5** Predicted vs. measured plot from the PLS regression of emulsion stability ($E_{crit}$) based on the NIR spectra. (From Aske, N.; Kallevik, H., Sjöblom, J. *J. Petrol. Sci. Engin.* **2002**, *36*, 1–17.)

from NIR spectra. The predicted to measured emulsion stability is presented in Figure 12.5. NIR spectra contain information on both the aggregation state of asphaltenes and on chemical composition. This may explain the reason for its good predictive power for the $E_{critical}$ values.

#### *12.2.3.1.4 High-Pressure Study of Asphaltene Aggregation*

Asphaltenes tend to self-associate depending on solvent, pressure, and temperature conditions. Generally, aliphatic solvent conditions and pressure reductions will increase asphaltene aggregation size. Under increasingly unfavorable solvent condition, asphaltenes aggregate and eventually precipitate as large asphaltene flocculates. The asphaltene precipitation onset gives important information about the solubility of the asphaltenes in a given hydrocarbon system. Such measurements are carried out by titrating the system with an n-alkane, while measuring some physical property (e.g., light absorbance, viscosity, electrical conductivity), which shows a distinctive discontinuity at the precipitation onset [23]. NIR is an excellent and popular method for measuring the asphaltene precipitation onset [24–27]. As shown in Figure 12.6, the optical density of the system decreases as a consequence of dilution, until the precipitation threshold is reached. At that point the apparent absorbance increases due to light scattering of the precipitating asphaltenes. Aske and co-workers [28] have investigated the asphaltene aggregation behavior from crude oils and model systems under high pressure. Model systems and the crude oil were pressurized to 100 and 300 bar respectively. The systems were then depressurized in steps, and the resulting NIR spectra were recorded at each pressure level and analyzed with multivariate analysis. The asphaltene precipitation onset pressure was identified from increased optical density due to light scattering. By reducing the pressure even further, the bubble point was detected from the subtle drop in absorbance due to gas evolution. The reversibility of the asphaltene aggregation was studied for the crude oil and a model system by repressurizing the systems stepwise from the bubble point to the original pressure. The systems were then left to equilibrate for several hours.

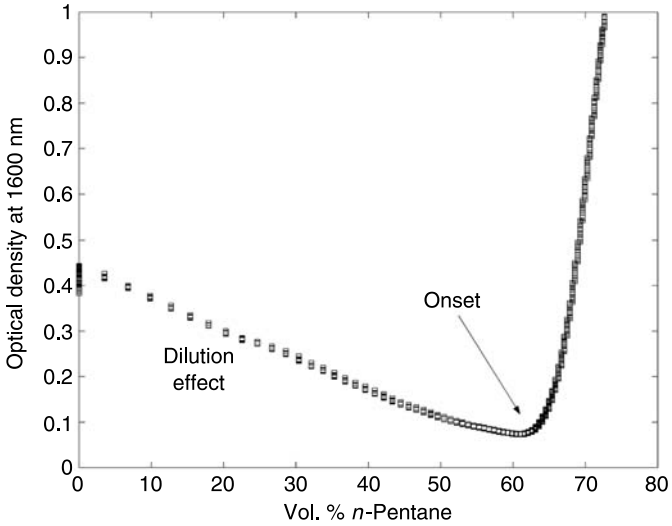


**FIGURE 12.6** Asphaltene precipitation onset measured by NIR spectroscopy.

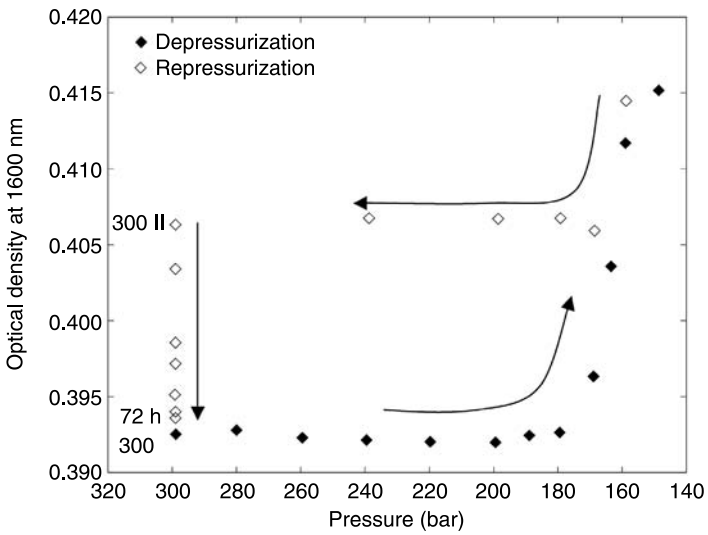


**FIGURE 12.7** Asphaltene aggregation and reversibility of crude oil studied by high-pressure NIR. (From Aske, N.; Kallevik, H.; Johnsen, E. E., Sjöblom, J. *Energy & Fuels* **2002**, *16*, 1287–1295.)

Here, we will focus on the part of the study dealing with repressurization. Figures 12.7 and 12.8 show the recorded optical density at 1600 nm of the crude oil and the model system during the pressure cycle.

For the crude oil, considerable redissolution of the aggregates was seen when increasing the pressure from 150 to 170 bar, as reflected by the decreased optical density. After 72 h the aggregate size had practically returned to its original state. For the model system, the aggregates seemed to redissolve steadily during the depressurizing, but came to a stop after approximately

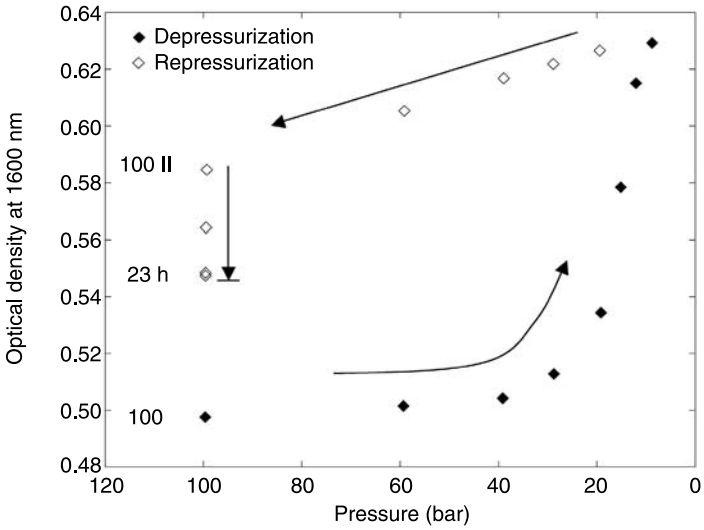


**FIGURE 12.8** Asphaltene aggregation and reversibility of model system studied by high-pressure NIR. (From Aske, N.; Kallevik, H., Johnsen, E. E.; Sjöblom, J. *Energy & Fuels* **2002**, *16*, 1287–1295. Model system: 1.2 wt % asphaltenes; 35 wt % pentane in toluene.)

23 h at the original pressure of 100 bar. While the asphaltene aggregation of the crude oil was more or less completely reversible, the asphaltene aggregation in the model system was only partially reversible. The authors explained the different behavior of the crude oil and the model system to be caused by the lack of dispersing resins during the repressurization of the model system. This study is a typical example of the power of NIR spectroscopy to monitor physical changes in crude oil systems.

#### *12.2.3.1.5 NIR Study on the Dispersive Effect of Amphiphiles and Napthenic Acids on Asphaltenes*

Auflem and co-workers [29] showed the ability of NIR to follow the disintegration of asphaltene aggregates upon addition of chemicals or indigenous crude oil components. In order to hinder asphaltene deposition, the petroleum industry injects large volumes of chemicals into reservoirs and pipelines. These chemicals are supposed to imitate the indigenous resin fraction, by dispersing the asphaltenes in the hydrocarbon mixture as discussed earlier in this chapter. In addition to the direct problems concerning asphaltene deposition in process equipment, the stability of water-in-oil emulsions will be strongly dependent on the asphaltene aggregation size and state [30,31]. The asphaltene aggregation state is monitored with NIR spectroscopy after addition of chemicals known to efficiently disperse asphaltenes through different interaction mechanisms depending on the additive. The results showed that additives, which are efficient in replacing hydrogen bonds in asphaltene aggregates, possess dispersive power and can serve as inhibitors. Commercial blends gave the best results.

#### *12.2.3.1.6 Asphaltene Destabilization*

Recently, in a study concerning the potential for hydrate plugging, crude oils washed with a strong alkaline solution (pH 14) showed much higher water-in-oil emulsion stability than the

**TABLE 12.2**
**Asphaltene Precipitation Onset (ml n-Heptane/g Crude Oil) Measured by NIR Spectroscopy**

| | Original | pH14 washed |
|---|---|---|
| Crude oil A | 7.0 | 4.2 |
| Crude oil B | 3.2 | 2.3 |
| Crude oil C | 3.9 | 3.2 |
| Crude oil D | 5.0 | 1.7 |

original crude oils [32]. The pH 14 wash extracts the most polar resins, typically napthenic acids and phenols. As mentioned earlier, these compounds play an important role in solubilizing the asphaltenes. Removing them should cause the asphaltenes to precipitate earlier when titrating the crude oil with an n-alkane. The asphaltene precipitation onset was measured by NIR spectroscopy. As shown in Table 12.2, the asphaltenes in the pH 14 washed crude oils precipitated *earlier* than the asphaltenes in the original crude oils. NIR can be used for the initial screening of a large number of chemicals for asphaltene inhibition.

## 12.3 PHYSICOCHEMICAL PROPERTIES

### 12.3.1 Critical Electric Field as a Measure of Emulsion Stability

Electro-coalescers are commonly used in the oil industry to enhance the separation of water from crude oil. The electro-coalescer applies an electric field of 1 to 10 kV $cm^{-1}$ through the flowing water-in-oil emulsion to enhance the flocculation and coalescence of the dispersed water droplets [33]. Basically, the water droplets increase their sizes through the electro-coalescer, and thereby the water sedimentation rate is increased [34,35]. There is a variety of factors influencing the electrically induced coalescence, such as the dielectric properties of the dispersed and the continuous phase, the volume fraction of the dispersed phase, conductivity, size distribution of the dispersed droplets, electrode geometry, electric field intensity, the nature of the electric field (AC or DC), etc. [36–38].

An electric field cell containing a small volume of sample has recently been developed for the determination of emulsion stability [22]. The method is similar to the one employed by Kallevik et al. [39]. The cell consists of two brass plates separated by a 0.5 mm Teflon plate (Figure 12.9). The Teflon plate has a 10 mm diameter hole in the center so that a small sample of emulsion can be injected between the two brass plates. The brass plates are connected to a power supply (Agilent Model 6634B). The power supply can increase the voltage stepwise and measure the current passing through the emulsion. A sudden increase of the current will indicate that the electric field has broken the emulsion and that there will be a free transport of ions between the electrodes. The corresponding electric field is the E-critical value.

Figure 12.10 illustrates how emulsions behave under the influence of the applied field. When no field is applied, the water droplets are randomly distributed according to Stokes law of sedimentation and Brownian motion. In addition, some degree of droplet flocculation may be present. As the field increases, the droplets line up between the electrodes due to polarization of the aqueous

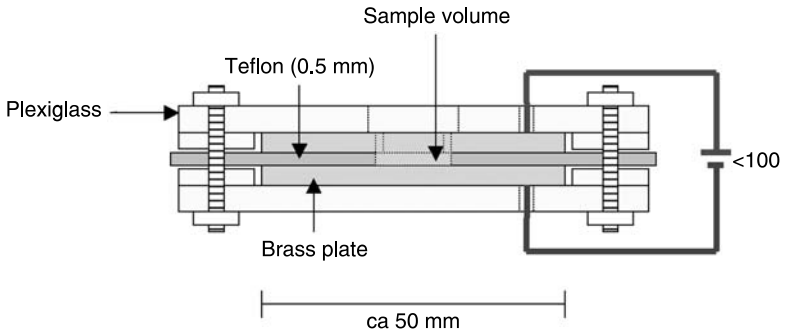


**FIGURE 12.9** The critical electric field cell.

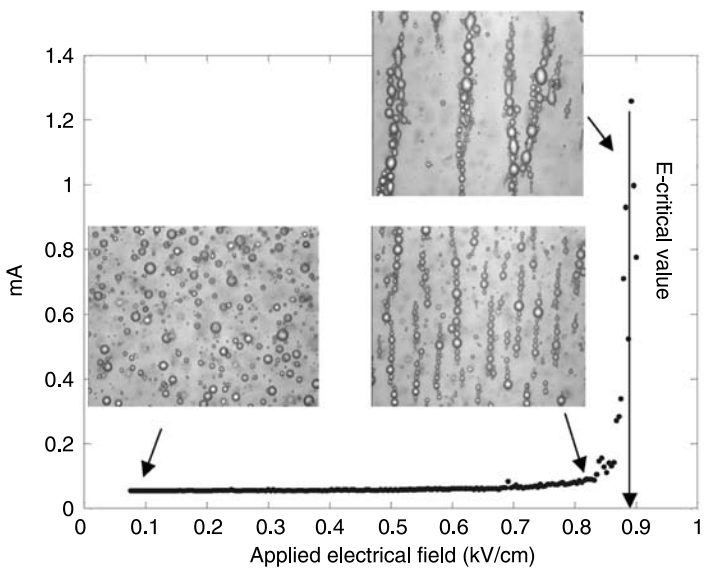


**FIGURE 12.10** Behavior of w/o emulsions in an external electric field.

droplets containing electrolyte. Finally, at some point, the applied electric field causes irreversible rupture of the interfacial films between the droplets [33]. The droplets coalesce, resulting in a water-continuous bridge between the electrodes. The ions of the water phase contribute to a sudden increase in the conductivity. The emulsion stability is hence defined as the strength of the field when the conductivity suddenly rises.

#### 12.3.1.1 Applications

The critical electric field technique can only be used for emulsions where the continuous phase is an insulator and the dispersed phase has conducting capacity. Hence it can be used for measuring the stability of water-in-oil emulsions, but not for oil-in-water emulsions.

One question that often arises when facing an emulsion problem is: what factors are causing the stabilization of the emulsion? This is an important question in order to select the right remedy.

The break-up of an emulsion can be simplified in two steps: first the droplets flocculate due to weak attraction forces between the droplets, and secondly they coalesce which depends on the physicochemical properties of the surrounding membrane. The flocculation step is controlled by different factors like the attraction potential between the droplets and the viscosity of the continuous phase between the droplets, i.e., the crude oil, and the droplet sizes of the dispersed water droplets. The coalescence step is controlled by natural surfactants within the crude oil, indigenous compounds like naphthenic acids, resins, and asphaltenes, stabilizing the interfacial film on the water droplets and giving it the crucial physicochemical properties. Aske et al. [40] investigated which analytical and physicochemical parameters contribute to emulsion stability properties. Using multivariate data analysis, they correlated emulsion stability measured by the critical electric field technique to physicochemical parameters such as molecular weight, density, viscosity, interfacial tension, interfacial elasticity, total acid number (TAN), and SARA fractions for a crude oil matrix consisting of 21 samples. They concluded that the asphaltene content, state of asphaltene aggregation, and interfacial elasticity were the most important factors with regard to emulsion stability. The crude oil matrix used by Aske et al. was mostly made up of conventional crude oils. In our group we are continuing this work using a crude oil matrix of heavy crude oils [41].

Earlier work includes also the evaluation of the emulsion stability by means of the critical electric field technique in order to study D-phase stabilization in combination with asphaltene particles in acidic heavy crude oil systems [42]. The background for this study is to compare different stability mechanisms. It is well known that oil-continuous emulsions can be stabilized by multiple layers of surfactant instead of only a monolayer. In an equilibrium situation this corresponds to a sample location in a three-phase area where two solution phases (L1 and L2) are in equilibrium with a lamellar liquid crystalline phase (so-called D phase). This situation is of relevance in crude oil systems with high levels of naphthenic acids. In order to simulate the situation in a high aphaltenic crude we also combined the D-phase stabilization with asphaltene particles. In this way we could create situations where the stability level rose several times reflecting the combined influence of multiphase stabilization and organic particles.

Recently in our group, we have used the critical electric field technique to study the effect of temperature on the emulsion stability. We have also investigated how different kinds of modifications on crude oils, like deasphalting, dilution, and alkaline washing, affect the emulsion stability.

Heavy crude oils are known to be very viscous. For the line up of the droplets between the electrodes in the critical electric field cell, the viscosity of the continuous phase should be one of the time-limiting factors. In order to test how the emulsion stability is affected by changing the viscosity, five crude oils were diluted in different ratios with a heptane–toluene mixture (70:30 vol%) [41]. The diluted crude oils were then mixed with 30% water containing 3.5 wt% NaCl and the emulsion stability was measured by the critical electric field cell. Figure 12.11 shows that, generally, for the five crude oils, the emulsion stability decreases as the viscosity is decreased by dilution. However, as the crude oils are diluted, the concentration of surface active compounds like resins and asphaltenes is also decreasing, which will also affect the emulsion stability. Likewise, the interfacial tension and interfacial elasticity will also change as a result of the dilution. The most interesting information from Figure 12.11 is what happens to crude oils 3 and 4. At high viscosity their corresponding emulsions show high stability, but as we increase the dilution (decreasing the viscosity), the stability drops, but levels off at a certain level, independently of the viscosity. In this region, where the E-critical value is fairly stable, the line up of the water droplets cannot be the limiting step for the break-up of the emulsion.

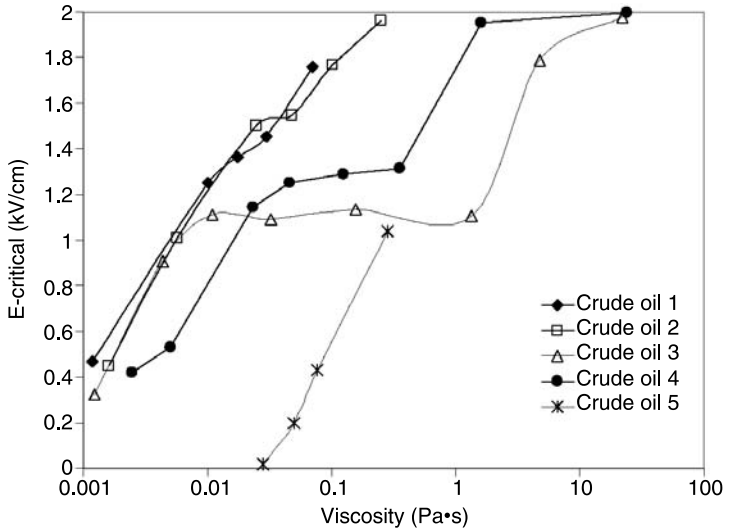


**FIGURE 12.11** Emulsion stability, measured by means of critical electric field technique, as a function of the viscosity of the crude oil, for five different oils. The viscosity was changed by dilution of the different crude oils by a heptane–toluene mixture (70:30 vol%).

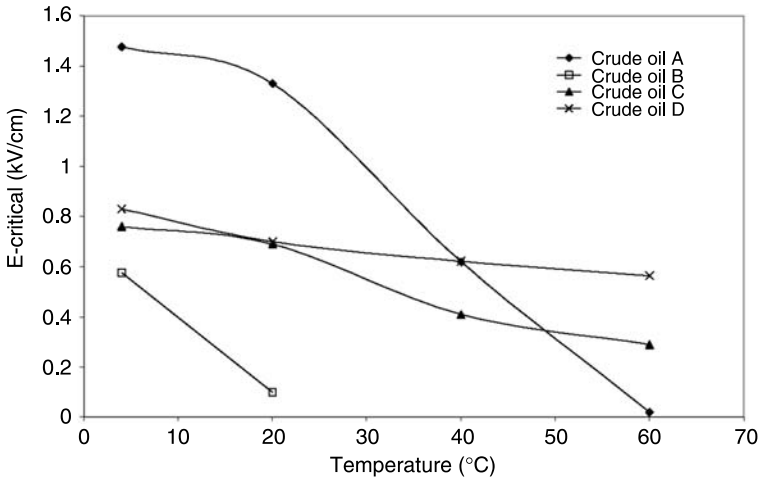


**FIGURE 12.12** Emulsion stability, represented by the critical electric field, E-critical, as a function of temperature for four different crude oils.

Another important aspect of emulsions is how they are affected by temperature. Figure 12.12 shows the emulsion stability, by means of the critical electric field, as a function of the temperature for four crude oil systems [32]. Prior to making the emulsions, the crude oil and water were heated/cooled to the appropriate temperature. The critical electric field cell was also kept at the same temperature as the emulsions. The results show that there is a big difference in the temperature dependence on the emulsion stability. Viscosity measurements showed that crude

**TABLE 12.3**
**Water in Oil Emulsion Stability Measured by the Critical Electric Field Cell for Original and Modified Crude Oils. Watercut: 30%. T = 20 °C**

| | E-critical (kV/cm) | | |
|---|---|---|---|
| | Original | Deasphalted | pH 14 |
| Crude oil A | 1.3 | 0.03 | 1.9 |
| Crude oil B | 0.1 | 0 | 1.8 |
| Crude oil C | 0.7 | 0 | 3.0 |
| Crude oil D | 0.7 | 0.7 | 1.9 |

oils A and B contained waxes, A most, with a wax appearance temperature around 20 to 25 °C, while crude oils C and D contained little or no wax. Crude oils C and D, however, contained much more asphaltene than crude oils A and B. The results from the critical electric field cell are in agreement with the crude oil characteristics. Crude oil A, being a waxy crude, shows high emulsion stability at low temperatures, but as the temperature increases, the wax melts and the emulsion stability drops rapidly. Crude oil B contains less wax than crude oil A, and shows less stability than crude oil A. For crude oils C and D, the emulsion stability decreases less than for the two waxy crude oils, and the emulsions are most likely stabilized by asphaltenes, resins, and/or inorganic fines.

The four crude oils were modified in two different ways; either by deasphalting using n-pentane or by a pH 14 treatment. The pH 14 treatment extracted the most polar resins in the crude oils, typically compounds containing naphthenic acids or phenols. Emulsion stability of the original and modified crude oils was measured by the critical electric field technique. The results in Table 12.3 show that deasphalting crude oils A, B, and C resulted in very unstable emulsions. As mentioned earlier, crude oils A and B contained wax, and Figure 12.12 showed that the wax was the stabilizing component in the emulsions. FTIR of the precipitated asphaltenes showed wax structures in the asphaltenes from crude oils A and B, meaning that the wax was also removed from the crude oil during the deasphalting. For crude oil C one can draw the conclusion that the asphaltenes are the main stabilizing component, as removing those results in an unstable emulsion. For crude oil D, however, removing the asphaltenes has no effect, meaning that there must be other stabilizing mechanisms other than wax and asphaltenes for this crude.

Removing acidic compounds from the crude oils has a large effect on the emulsion stability. All the pH 14 washed crude oils formed much more stable emulsions than the original crude oils. The polar resins play a very important role in stabilizing the asphaltenes. By removing the most polar resins we have disturbed the interaction pattern between the resins and the asphaltenes, and the asphaltenes left in the crude oil have a much higher propensity to stabilize emulsions. This is in accordance with several studies [29,31,43].

### 12.3.2 Determination of the Rheological Characteristics of a W/O Interface

Interfacial rheology is the measurement of the elasticity and viscosity of interfacial films that form on liquid surfaces. These properties play an important role for the stability of water-in-crude-oil emulsions and the mechanism of demulsification. It has been shown that when indigenous crude oil components adsorb onto an interface between oil and water they can protect the interface against coalescence [30,31]. In short, when the interface is stressed, the uneven distribution of interfacially active components will create tension gradients on the interface that will oppose the

strain, i.e., the Gibbs–Marangoni effect. The interface will hold elastic properties protecting the interface from coalescence. Determination of the rheological properties of an interface can be undertaken with dilational stress where the interfacial resistance to changes in area is monitored. Measurements are made by simultaneously analyzing the interfacial tension and surface area of a drop which is periodically perturbed. A fresh oil droplet is created from a needle immersed in water and its volume is modulated by a syringe pump to give a sinusoidal variation of the surface area of the drop.

$$\Delta A = A - A_0 = A_a \sin(\omega t) \tag{12.3}$$

$A_a$ is the area amplitude and $A_0$ is the equilibrium area. The drop shape remains constant. The principle of the method is to monitor the change in interfacial tension as a result of processes trying to re-establish equilibrium of the interface. The dynamic interfacial tension is estimated using axisymmetric drop shape analysis as presented in Section 12.3.4.

$$\Delta\gamma = \gamma - \gamma_0 = \gamma_a \sin(\omega t + \theta) = \gamma_a \sin(\omega t)\cos\theta + \gamma_a \cos(\omega t)\sin\theta \tag{12.4}$$

Here $\gamma_a$ is the tension amplitude and $\gamma_0$ is the equilibrium interfacial tension. The phase angle $\theta$ is shown in Figure 12.13 and can be estimated by a phase comparison between the variation in area and the response in tension. The interfacial dilational modulus $E$ describes the response of an interface to local compression and expansion and is defined as the interfacial tension increment per unit fractional change in the interfacial area [40].

$$E = \frac{d\gamma}{d\ln A} \tag{12.5}$$

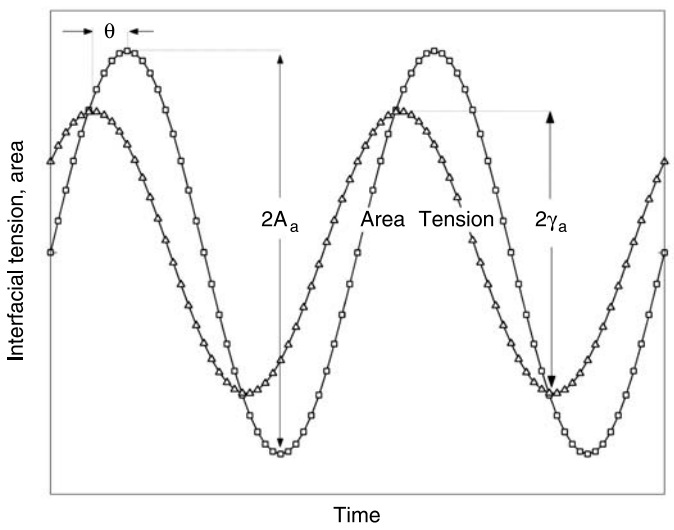


**FIGURE 12.13** Time dependent relationship between area and interfacial tension during a dilational rheology experiment.

When analyzing the relaxation processes at or near the interface between oil and water, we expect the rheological properties of the interface to be viscoelastic rather than pure elastic. The interfacial dilational modulus is a complex function of the angular frequency of oscillation $\omega$ [44].

$$E^* = E_d + i\omega\eta_d = E' + iE'' \tag{12.6}$$

$E_d$ is known as the interfacial dilational elasticity whereas the interfacial dilational viscosity $\eta_d$ corresponds to the dynamic viscosity in an ordinary bulk oscillatory rheology experiment. The complex dilational modulus $E^*$ may be written as the sum of two contributions. An elastic component accounting for the recoverable energy stored in the interface (the storage modulus $E'$) and a viscous component accounting for the energy lost through relaxation processes (the loss modulus $E''$). The storage modulus is in phase with the modulation and the loss modulus is 90° out of phase. By using the Gibbs definition of elasticity (Equation 12.5) with insertion of the variation in drop area (Equation 12.3) and the corresponding variation in interfacial tension (Equation 12.4), the complex interfacial dilational modulus $E^*$ can be expressed as:

$$\begin{aligned} E^* &= \frac{\Delta\gamma}{\Delta \ln A} = \frac{\Delta\gamma}{\Delta A/A_0} \\ &= \frac{\gamma_a \sin(\omega t)\cos\theta + \gamma_a \cos(\omega t)\sin\theta}{A_a \sin(\omega t)/A_0} \\ &= \frac{\gamma_a}{A_a/A_0}\left(\cos\theta + \frac{\cos(\omega t)}{\sin(\omega t)}\sin\theta\right) \\ &= |E|\cos\theta + i|E|\sin\theta \end{aligned} \tag{12.7}$$

where

$$|E| = \frac{\gamma_a}{A_a/A_0}$$

With the analyzed "movie" in hand, there are several approaches for the determination of the rheological parameters. One includes a Fourier transformation of the interfacial tension waveform inside subdivisions of the "movie" [45].

$$\begin{aligned} E^* &= \frac{\mathrm{FT}\Delta\gamma(t)}{\mathrm{FT}(\Delta A/A_0)(t)} \\ &= \frac{\int_0^\infty \Delta\gamma(t)\exp(-i\omega t)dt}{(\Delta A/A_0)i\omega} \end{aligned} \tag{12.8}$$

The $E'$ and $E''$ moduli can be determined as the real and the imaginary part of Equation 12.8. Figure 12.13 may represent such a subdivision including two cycles. The duration of each subdivision is a tradeoff between smoothness (more cycles results in less variance) and time resolution (less cycles gives quicker response). The frequency component corresponding to the modulation can be easily picked out from the spectrum and other frequencies (noise) rejected.

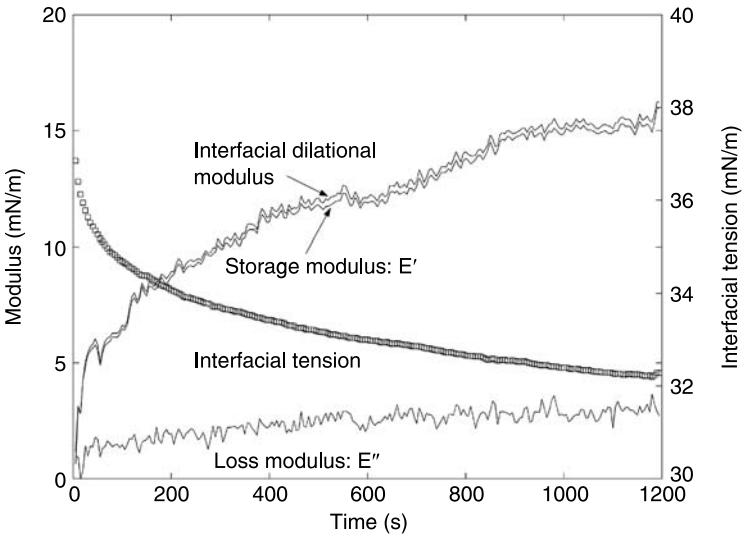


**FIGURE 12.14** Dynamic pendant drop experiment of diluted (heptane/toluene equal volumes) Brazilian heavy crude oil immersed in water (3.5 wt% NaCl). Frequency of oscillations is 0.1 Hz. $\theta \sim 12°$.

Figure 12.14 shows the interfacial tension response of a sinusoidal oscillation of a diluted Brazilian oil against water (3.5 wt% NaCl). Each point represents a Fourier transformed subdivision of the interfacial tension profile. The interfacial tension decays from the initial tension of a pure interface to 32 mN/m, 20 min after drop formation. Storage and the loss moduli are also included. The loss modulus stays essentially constant while the storage modulus increases greatly when the interface is organized with interfacially active crude oil components. The interface is mainly elastic (close fit between $E'$ and $E$) but it also holds some viscous properties reflected by a non-zero $E''$ and a phase angle: $\theta \sim 12°$.

#### 12.3.2.1 Applications

Aske and co-workers investigated the interfacial rheology of water–crude oil systems [40]. An oscillating pendant drop apparatus was used in the systematic characterization of 21 crude oil and condensates with respect to interfacial elasticity. The elasticity modulus of the interface after 1000 sec was reported. These experiments were supplemented by near-infrared spectroscopy (optical density at 1600 nm) to keep track of the asphaltene aggregation state in the oil phase.

Results presented in this example are the elasticity modulus with corresponding optical density of one of the crude oils, a West African crude oil with 1 wt% asphaltenes. The crude oil was diluted to 3 different concentration levels (ml oil/ml solvent) with solvents of heptane and toluene. The effect of crude oil concentration and solvent composition will be discussed with reference to Figure 12.15, showing the elasticity modulus of the oil–water interface and the optical density of the oil phase.

In poor solvents (high heptane content) the interfacial elasticity decreased with increasing oil concentration. In good solvents the interfacial elasticity generally increased with oil concentration. From the optical density the formation of larger aggregates is seen to be much more dominating in poorer solvents. The lowering of the interfacial elasticity appeared to be caused by the formation

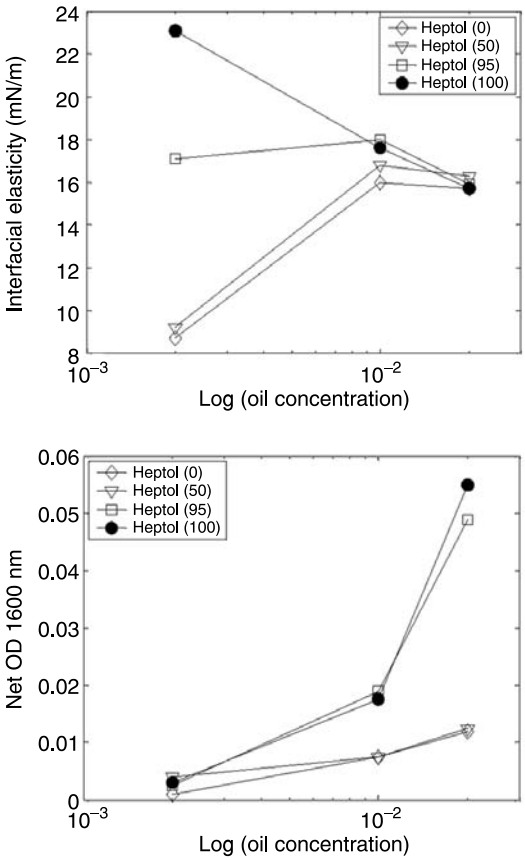


**FIGURE 12.15** Elasticity modulus of an interface between diluted crude oil and water (3.5 wt% NaCl) (top). Corresponding optical density of the oil phase is also reported (bottom). The number in the legend indicates the heptane content of the solvent (vol%).

of larger asphaltene aggregates. At the lowest oil concentration, the highest elasticity of the interface was obtained in the poorest crude oil surfactant solvents. In such solvents the interfacial activity of resins and asphaltenes were high, and asphaltenes appeared to be in a favorable aggregation state. At higher oil concentrations this effect of interfacial activity seemed to be opposed by the formation of asphaltene aggregates.

This study by Aske and co-workers [40] demonstrates that measurements of interfacial rheological properties of crude oil systems are highly dependent both on oil concentration and of the solvent used for dilution. The results are consistent with the asphaltene aggregation model proposed by Kilpatrick and co-workers [30,31]. They found that precipitated asphaltenes had a lower ability to form elastic interfaces. This was attributed to lower interfacial activity of such precipitated aggregates and possibly high amounts of defects in films of precipitated material. It should be mentioned that the measurements by Kilpatrick et al. were performed according to other measurement principles.

### 12.3.3 The Langmuir Technique

#### 12.3.3.1 Background

In studies of insoluble monolayers on liquid surfaces, the parameter of greatest interest and the one usually measured is the difference in surface tension between a clean or pure liquid surface and one covered with a film. This quantity is called the surface pressure and denoted by a Greek pi ($\Pi$):

$$\Pi = \gamma - \gamma_0 \tag{12.9}$$

where $\gamma$ is the surface tension in the absence of a film and $\gamma_0$ the tension of the film-covered surface. The surface tension of water is 73.05 mN/m at 18 °C and atmospheric pressure [46]. Hence the maximum possible surface pressure for a monolayer on a water surface at this temperature is 73.05 mN/m.

The Langmuir technique is used in order to characterize film properties of surface-active materials. The instrumentation consists of a shallow rectangular container (trough) in which the liquid subphase is added, whereupon the film is spread. The barriers, for manipulation of the film, rest across the edges of the trough (Figure 12.16(a)). The surface pressure is measured by means of the Wilhelmy method [47–49]. Modification of the trough design has made it possible to carry out the same kind of experiments on a liquid/liquid interface, i.e., the oil/water interface. In this case the trough is a "double trough" (Figure 12.16(b)) where the barriers contain holes to allow the flow of the light phase as the compression of the interphase proceeds. The Wilhelmy plate is first placed in the aqueous phase, and then the oil phase is added until the plate is totally immersed.

The most common way of presenting the data obtained from the Langmuir technique is a plot of surface pressure as a function of surface area. The measurements are carried out at a constant temperature and are known as surface pressure/area isotherms. The film is compressed at constant rate by the moving barriers while the surface pressure is continuously monitored. As the surface area is reduced from its initial high value a series of different regions indicating different states of the monolayer is observed. Analogously to bulk matter these states are characterized as gas-like, liquid-like, and solid-like [50,51]. At small surface areas the monolayer will collapse;

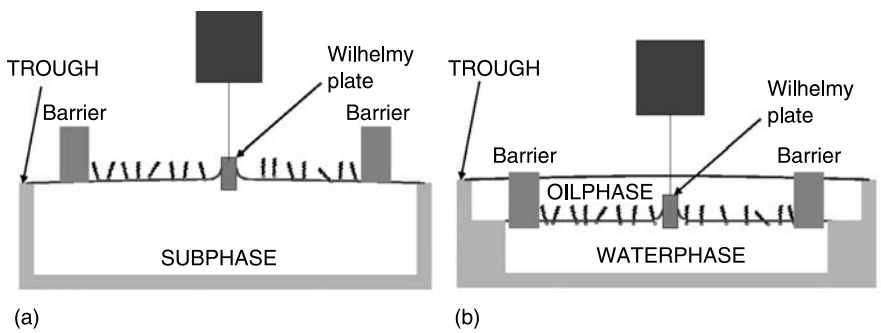


**FIGURE 12.16** Illustration of the different Langmuir troughs. (a) Liquid–air surface trough. (b) Liquid–liquid interfacial trough.

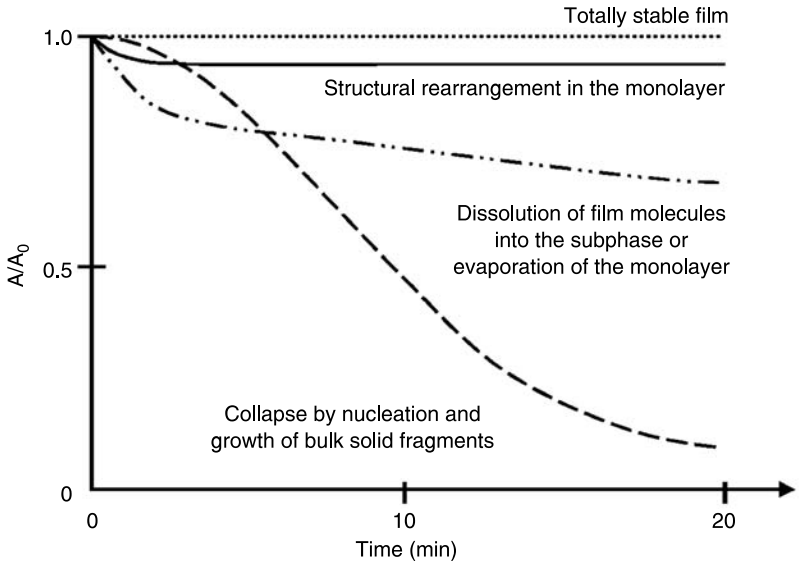


**FIGURE 12.17** Relaxation curves at constant surface pressure for monolayers of different stability.

the collapse pressure is the highest surface pressure to which a monolayer can be compressed without a detectable movement of the film molecules and formation of a new phase. The variation and complexity of the monolayer behavior is a result of the different intermolecular interactions in the film and between the film and the subphase. This implies that the changes in interaction forces are related to the packing of the molecules in the two-dimensional plane [48,49].

In order to be able to interpret a surface pressure/area isotherm, the film stability has to be characterized. The stability of a monolayer is studied by measuring the area loss at constant surface pressure or the decrease in surface pressure at constant area. The different shapes of the relative area isotherms in Figure 12.17 illustrate the most common destabilization mechanisms [52–55].

#### 12.3.3.2 Applications

Studies of film properties of asphaltenes and resins provide information on the compressibility and stability of monolayers consisting of these indigenous crude oil components. This kind of information might be virtually correlated to formation of stable emulsions. Hence, a rigid film on the emulsion droplets prevents coalescence while a highly compressible film is more easily ruptured, leaving the droplets free to coalesce.

By means of the Langmuir technique, asphaltenes are found to build up close-packed rigid films, which give rise to quite high surface pressures. Resin films, on the other hand, are considerably more compressible (Figure 12.18) [56]. This may explain the experimental observations showing that asphaltenes are able to stabilize crude oil based emulsions, while resins alone fail to do so. Singh and Pandey [57] also concluded that a high interfacial pressure correlated with high w/o emulsion stability. Adding asphaltenes and resins together into a mixed film, the properties gradually change from a rigid to a compressible structure as the resin content is increased. The more hydrophilic resin fraction starts to dominate the film properties due to the higher affinity towards the surface.

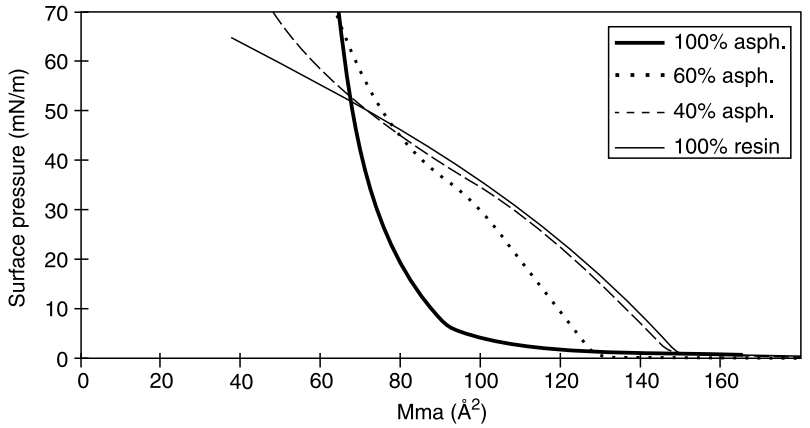


**FIGURE 12.18** $\Pi$-A isotherms of asphaltene/resin mixtures spread from pure toluene on pure water (bulk concentration = 4 mg/ml).

The influences of chemical additives on asphaltene films on water surface and at oil/water interface have also been studied by means of the Langmuir technique. This was done in order to view the interaction between demulsifiers added and asphaltenes, and to show the importance of this on emulsion stability.

Highly compressible resin films alone will not stabilize a crude oil emulsion. Related to this, demulsifiers, which form films of low rigidity and high compressibility, should be most efficient. When used as demulsifiers, the efficiency depends on the ability of the chemicals to interact with and modify the film built up by asphaltene particles.

Addition of demulsifiers of high molecular weight in the asphaltene film gave the isotherms in Figure 12.19 [58]. Chemical G is highly effective with respect to increased compressibility together with a reduced rigidity. The effect of this kind of manipulation of the asphaltene film is similar to the effects observed when resins are mixed together with asphaltenes (Figure 12.18).

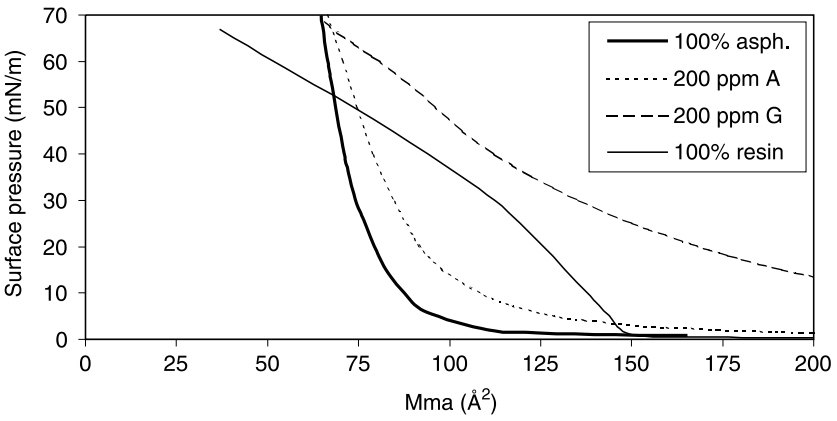


**FIGURE 12.19** $\Pi$-A isotherms of mixed monolayers of asphaltenes and two different demulsifers on pure water. The mixed monolayers are compared with the pure asphaltene and the pure resin film.

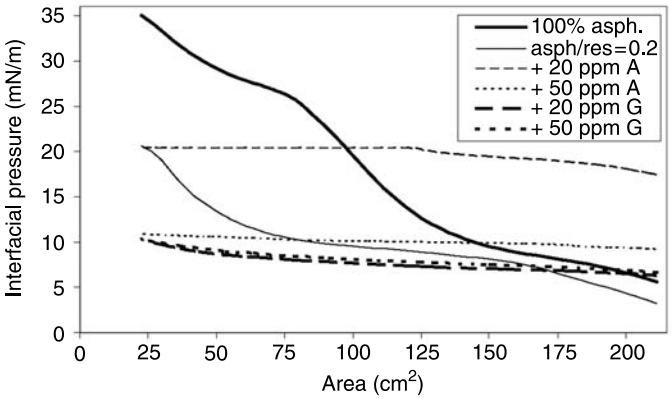


**FIGURE 12.20** Interfacial pressure isotherms of films formed between water and oil containing different ratios of asphaltenes and resins or asphaltenes and demulsifiers.

However, the concentration needed to achieve the same effects is considerably lower when demulsifiers are used instead of resins. Demulsifier A has a quite small influence on a film of asphaltenes.

From film studies above one can conclude that the best candidates for emulsion breaking should be G. However, the efficiency depends not only on the direct influence of chemical additives within the film, but also on the ability of demulsifiers to reach the w/o interface in an emulsion (diffusion through the fluid). This is a critical step regarding the effective concentration of demulsifiers at the interface. These aspects make it difficult to undertake a direct comparison between influence of demulsifier in Langmuir surface films, where all demulsifier molecules are implanted in the film (2-D), and in real emulsions with a hydrocarbon environment (3-D).

In order to represent more realistic emulsion conditions, Langmuir interfacial films adsorbed at the oil/water interface were analyzed [58]. The isotherms given in Figure 12.20 illustrate some of the film properties of naturally occurring crude oil components adsorbed at the o/w interface.

The oil phase containing only 0.01 wt% asphaltene gives rise to a less rigid interfacial film than observed at the water surface (Figure 12.18). This is most likely due to the possibility for the hydrocarbon tails of the asphaltenes to orient towards the highly aliphatic oil phase, making the interactions between the film material, and, hence, the pressure increase during film compression, less extensive. In general interactions between the bulk phase and interfacial components are different to the water/air case.

Addition of resins to 0.01 wt% asphaltene solutions further reduces the adsorption of interfacially active components onto the oil/water interface, even if the total amount of naturally occurring surfactants is considerably higher in these oil phases. The reduction is seen as reduced pressure at constant interfacial area. These changes may be attributed to the ability of resins to disperse asphaltenes in the bulk oil phase, and thus prevent this heavy fraction from building up a stabilizing film between oil and water.

Introducing chemical additives together with asphaltenes in the oil phase may highlight the ability of these chemicals to prevent formation of relatively rigid asphaltene films at the oil/water interface. For concentrations higher than 20 ppm of chemical A there is no pressure increase during the compression. Hence, the film that is formed at the interface is highly compressible. So instead of increasing the pressure, the components will build up a multilayer, or the film

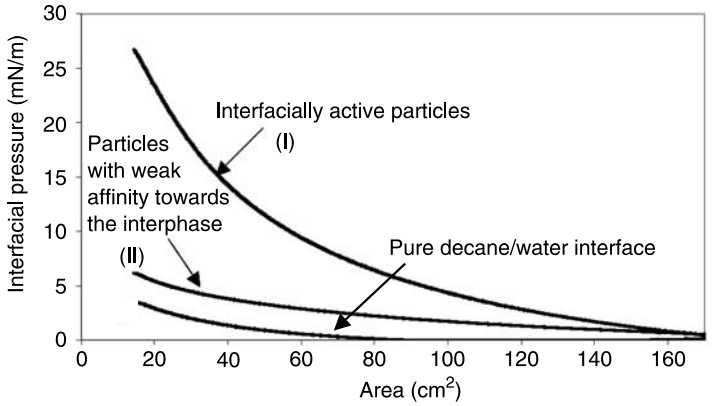


**FIGURE 12.21** Interfacial pressure isotherms of films formed between water containing different types of particles and an oil phase of pure decane.

may dissolve under the influence of compression. An increased inhibitor concentration reduces the interfacial pressure, but has no influence on the film behavior. The reduced pressure is probably due to a more complete cover of inhibitor at the interface. That is, fewer components from the asphaltene fraction are adsorbed together with the chemical additive when the inhibitor concentration becomes high enough.

The results obtained upon addition of demulsifier G are similar to those of A. However, G clearly increases the compressibility of the film even at low concentration. The difference between 20 and 50 ppm is quite small, so it is reasonable to believe that maximal efficiency resulting from the competing adsorption in a system like this is reached already at a concentration of 20 ppm of the oil phase. With 20 ppm or more G present, only small amounts of asphaltene will reach the interface.

The results obtained from the Langmuir interfacial film studies are important in explaining why certain chemicals are more effective as inhibitors than as demulsifiers. Obviously the inhibitor/asphaltene interaction is so strong in the bulk oil phase that the interfacial structures being gradually built up will no longer possess properties required to stabilize w/o emulsions.

Interfacial activity of particles might also be characterized by means of the Langmuir technique. Figure 12.21 illustrates the film properties of some naturally occurring reservoir particles adsorbed at the o/w interface (the particle sizes are the same for both fractions). The oil phase consists of pure decane while 1 wt% particles are added to the water phase. One of the particle fractions (type I) forms a relatively rigid film at the interface, while the other (type II) is more hydrophilic and remains dispersed in the aqueous phase. Studies of these particles' ability to stabilize emulsions have shown that type I particles are highly efficient emulsifiers, while type II particles will not form stable emulsion [59].

### 12.3.4 Pendant Drop Instrumentation/Interfacial Reactions

Interfacial tension (IFT) is a measurement of the cohesive energy present at an interface between two phases and is the most used parameter to characterize the dynamic properties of liquid adsorption layers. For a liquid in contact with a vapour, the molecules in the bulk phase are symmetrically surrounded by other molecules so that the molecular interactions in all directions

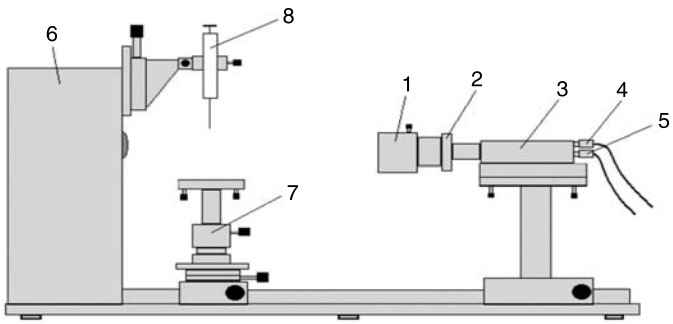


**FIGURE 12.22** A sketch of the CAM 200 equipment including its main components:
1: Camera lens zoom
2: Lens aperture adjustment
3: CCD camera
4: Light synchronizing cable
5: Video out cable
6: Light source and interface unit
7: Stage for sample
8: Syringe

are identical and the sum of all interacting forces is zero. At the liquid–vapour interface, however, the molecules are mainly affected by interacting forces from the liquid side, causing a net force towards the liquid bulk. The liquid molecules at the interface are thus "drawn" towards the bulk phase, which in turn cause a minimizing of interfacial area.

Hence, it is clear that the IFT increases with increasing intermolecular interactions. Thus, any factor which reduces the strength of these interactions, like increasing the temperature or introducing interfacially active molecules, will lower the IFT.

Several experimental techniques have been developed with the object of measuring IFT. This includes the technique of capillary rise, Wilhelmy's plate method, ring- and rotating drop tensiometry, the method of drop counting etc. In this section, the focus will be on the pendant drop technique, where liquid boundary tension is determined from the shape of drops without any direct contact.

The CAM 200 equipment is an optical instrument for contact angle and IFT measurements. The instrument includes a CCD video camera with telecentric optics, a frame grabber, and a LED based background light source. The resolution is 512 $\times$ 512 pixels and the frame interval is between 40 msec and 1000 sec. The LEDs are housed in a reflective sphere which integrates their light and directs it towards the sample. The light is also strobed and monochromatic, and all these features help to assure sharp images. Figure 12.22 shows the instrument including all its main components.

The pendant drop technique has a number of advantages compared to other techniques developed to determine IFT. Firstly, very accurate ($\pm$ 0.15% or less) boundary tension measurements can be made [60]. Furthermore, the measurements might be made rapidly and, since no direct contact exists, successive measurements may be performed without disturbing the interface.

The first studies involving the pendant drop technique were performed by measuring characteristic drop diameters and interpreting them to various tables [61]. Later, computer technology made it possible to obtain direct measurements through drop-shape analysis by coordinating the

data to suitable mathematical equations. Reviews of the theory behind the pendant drop technique have frequently been given in the literature [60,62–64].

A relation between drop shape and IFT might be given by introducing the classical Young–Laplace equation:

$$\Delta P = \gamma \left( \frac{1}{R_1} + \frac{1}{R_2} \right) \tag{12.10}$$

where $\Delta P$ is the pressure difference across the drop interface, $\gamma$ is the IFT and $R_1$ and $R_2$ are the radii of curvature. In the absence of external forces other than gravity, the difference in pressure is linear to the ascending forces:

$$\Delta P = \Delta P_0 + (\Delta \rho)\, g z \tag{12.11}$$

where $\Delta P_0$ is the pressure difference at a selected datum plane, $\Delta \rho$ is the difference in the densities of the two bulk phases, $g$ is the gravity, and $z$ is the vertical distance between the datum plane and a given point. A sketch of a pendant drop including symbols and dimensions is shown in Figure 12.23.

By combining Equations 12.10 and 12.11, and by introducing the geometrical correlations according to Figure 12.23, the following relation appears:

$$\frac{d\theta}{dS} = \frac{2}{R_0} + \frac{(\Delta \rho)\, g}{\gamma} z - \frac{\sin \theta}{x} \tag{12.12}$$

In most cases it is appropriate to transform $x$, $z$, and $S$ into the dimensionless coordinates $x'$, $z'$, and $S'$ by dividing by $R_0$. This results in the following three dimensionless first-order differential equations:

$$\frac{dx'}{dS'} = \cos \theta, \qquad \frac{dz'}{dS'} = \sin \theta, \qquad \frac{d\theta}{dS'} = 2 + \alpha \cdot z' - \frac{\sin \theta}{x'} \tag{12.13}$$

where the term $\alpha (= \dfrac{(\Delta \rho)\, g \cdot R_0^2}{\gamma})$ constitutes the shape factor of the pendant drop.

Thus, for any pendant drop where the densities of the two liquids in contact are known, the IFT might be calculated by iterating the above equations simultaneously.

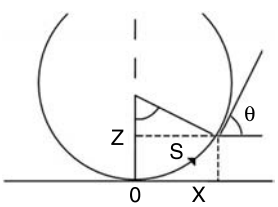


Geometrical correlations:

$R_2 = \dfrac{x}{\sin\theta}$, $\dfrac{dx}{dS} = \cos\theta$, $\dfrac{dz}{dS} = \sin\theta$

By definition: $\dfrac{1}{R_1} = \dfrac{d\theta}{dS}$

**FIGURE 12.23** A sketch of a pendant drop including some geometrical considerations.

#### 12.3.4.1 Applications

The CAM 200 equipment has recently been utilized to capture interactions between dissociated naphthenic acids and divalent cations across water–oil interfaces [65,66]. The work is related to crude oil production, where this process is assumed to be the origin of several problems, like stabilization of colloidal structures as well as formation of metal naphthenates through chemical reactions.

The naturally occurring naphthenic acids are complex mixtures consisting of aromatic and saturated rings connected by aliphatic chains [67,68]. The acids show polydispersity in stoichiometry and molecular weight [68–71] and due to the complex distribution of different structures, their physicochemical behavior is quite different from normal fatty acids. From an operational point of view, the naphthenic acids are causing several problems. Due to their amphiphilic nature, they may accumulate at interfaces and stabilize water/oil emulsions [72–74], which in turn causes enhanced separation problems. Dissociated carboxylic groups may also react stoichiometrically with metal cations present in the coproduced water to form metal naphthenates. Deposition of metal naphthenates in topside facilities like oil/water separators and desalters is becoming a serious problem in a number of fields with highly acidic crude, including fields in West Africa and in the North Sea [75,77,78].

Basically, there are two main approaches to how the naphthenic acids may react with cations to form metal naphthenate. The first is to consider bulk reactions between water soluble compounds and cations in the water phase. This was done by Havre [79], for example, who investigated the reaction between synthetic naphthenic acids and $Ca^{2+}$ at high pH by using near-infrared spectroscopy and by correlating changes in optical density to the growth of naphthenate particles. At normal operational conditions, however, only the low-molecular weight napthenic acids show significant solubility in water. The major part, constituting larger molecules, will preferably be oil soluble. According to this, and by considering the huge interfaces created when water is emulsified with the crude during the transportation from the reservoir to the topside, it is obvious that the contact and the interactions between the compounds *across* the interface may lead to a second approach, based on interfacial reactions.

The interest in interfacial behavior of carboxylic acids in combination with cations is not new and the topic has during the last decades been a subject of several studies. In that regard, a number of studies is carried out in order to establish correlations between pH and IFT [80–84] and to investigate effects of counter-ion binding on film stability [85–89]. However, few studies have been focused directly on interfacial reactions as a mean to understand naphthenate formation. The aim of the present work is thus to improve the understanding of how naphthenic acids of various structures may react across interfaces with different divalent cations. The experimental approach has been to correlate changes in dynamic IFT to plausible reaction mechanisms. In the following, some of the results obtained from the pendant drop study are discussed. The discussion is limited to the effect of adding divalent cations.

The experiments were executed by forming a pendant drop of a model oil (9:1 ratio of n-hexadecane and toluene) containing dissolved naphthenic acids in an alkaline aqueous solution. After reaching the initial equilibrium, divalent cations were added to the system. The IFT was measured both before, during, and after the addition of salt and then plotted versus time. The frame interval was set to one second for all experiments.

In Figures 12.24 and 12.25 examples are given for four different naphthenic acids, comprising two model compounds, Figure 12.24(a and b), and two acid mixtures from crude distillation,

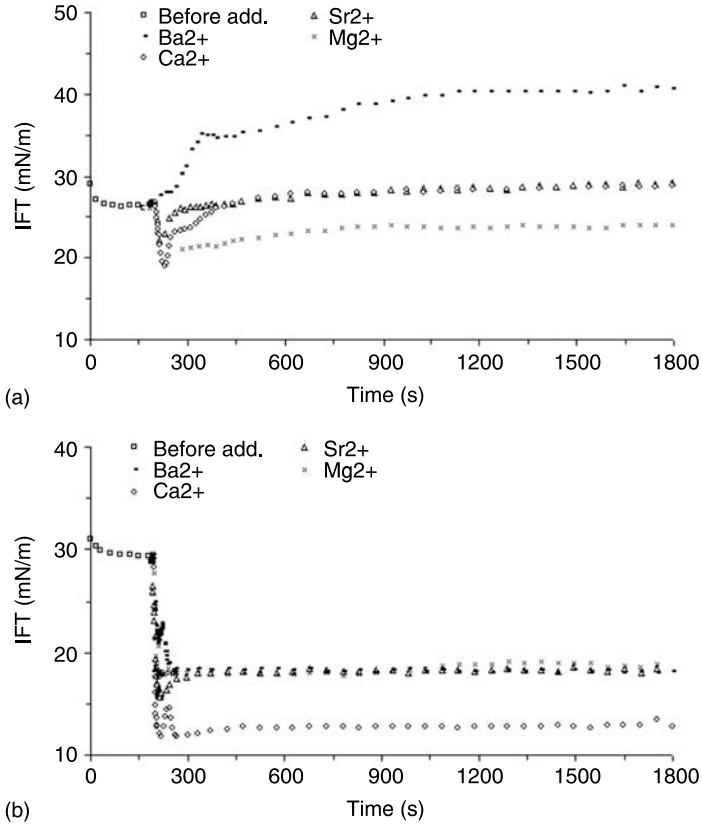


**FIGURE 12.24** Plots of interfacial tension versus time for two different model naphthenic acids in combination with various divalent cations. (a) *p*-(n-dodecyl) benzoic acid and (b) 4-n-dodecyl-cyclohexane carboxylic acid.

Figure 12.25(a and b). Table 12.4 shows an overview of all the structures whereas the experimental matrix is given by Table 12.5.

As indicated by the plots, the curves show quite different progress, depending on acid structure and type of added salt. The effect of adding different salts is more significant for the model acid comprising an aromatic ring (Figure 12.25(a)), than for the saturated model acid (Figure 12.25(b)). In a recent paper this was discussed as a result of dealing with compounds with different polarity [66]. Due to the aromatic ring, the unsaturated structures will penetrate deeper into the interface, enabling them to react chemically with the cations on the aqueous side of the interface. The dissimilarity in curve shapes is a result of adding cations with different sizes. The fact that the degree of hydration increases with decreasing ionic size will most likely influence the density of the cations at the interface. $Ba^{2+}$, which is less hydrated, will thus mainly form stoichiometric 2:1 complexes with the naphthenic acids. This will reduce the interfacial activity which is observed by an increase in IFT. $Mg^{2+}$, on the other hand, is highly hydrated and the cations will preferably be located in the water bulk, causing longer distance between the interacting compounds.

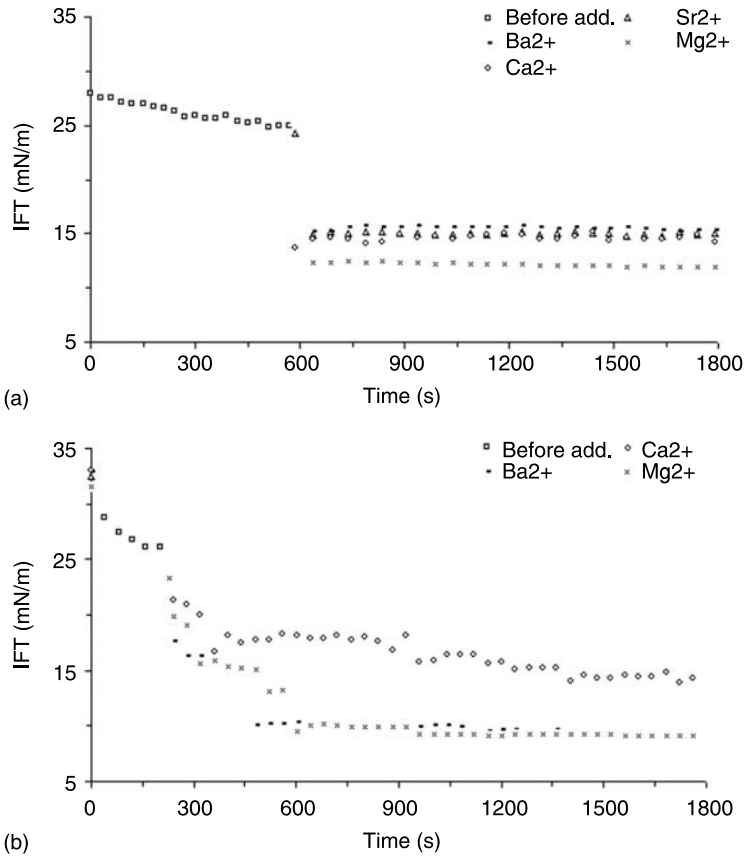


**FIGURE 12.25** Plots of interfacial tension versus time for two different indigenous naphthenic acid mixtures in combination with various divalent cations. (a) Fluka naphthenic acid mixture and (b) naphthenic acid mixture from a North Sea crude.

The permanent decline in IFT, which reflects coverage of more interfacial active compounds, is thus a result of electrostatic attracting forces exerted by $Mg^{2+}$ upon the carboxylate groups, or formation of positively charged monoacid complexes which remain at the interface due to high interfacial activity. If considering the latter, the question is whether the reaction with $Mg^{2+}$ will propagate through two steps or if the second reaction step is very slow.

Contrary to the systems involving the aromatic naphthenic acid, all the plots of the saturated structure show permanent lowering of the IFT (Figure 12.24(b)). This was explained in a similar way as for $Mg^{2+}$ in the former case: due to the hydrophobic saturated ring, the acid penetrates less into the interfacial layer and the distance between the interacting compounds across the interface might be too far to get a 2:1 formation of acid and cation. Now, since this is caused by the acid nature, all cations will affect the IFT in a similar way and the dominating mechanism should be electrostatic attractions.

Figure 12.25(a) shows the results from some experiments performed on the Fluka naphthenic acid, which is a commercial acid mixture. Due to high water solubility at pH 9.0, the experiments were carried out at pH 8.0. As indicated, addition of salt caused a sudden decline in IFT which

**TABLE 12.4**
**An overview of the naphthenic acids utilized in the experiments**

| Name | M (g/mol) | Naphthenic acid structure | Source |
|---|---|---|---|
| *p*-(n-dodecyl) benzoic acid | 290.4 | 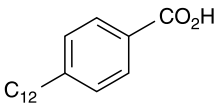 | Chiron AS |
| 4-n-dodecyl-cyclohexane carboxylic acid | 296.5 | 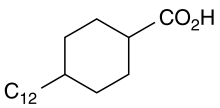 | Chiron AS |
| Fluka naphthenic acid | 250* | Mixture | Fluka |
| Naphthenic acids from a North Sea crude | 200 | Mixture | Statoil ASA |

*Average values calculated from total acid number (TAN).

**TABLE 12.5**
**The experimental matrix**

| Figure | pH | Acid conc. [M] | Conc. Ratio [$M^{2+}$/Ac] |
|---|---|---|---|
| 12-24a | 9.0 | $10^{-4}$ | 3/1 |
| 12-24b | 9.0 | $10^{-4}$ | 3/1 |
| 12-25a | 8.0 | $10^{-1}$ | 3/1 |
| 12-25b | 9.0 | $10^{-2}$ | 1/1 |

happened within 1 sec since no frame has been captured between the upper and lower state. The decline is also permanent for all systems, similar to the case involving the saturated model naphthenic acid. Analysis by FT-IR and NMR has also proved that the Fluka mixture mainly consists of saturated structures. Based on earlier statements, it is fair to suppose that the main mechanism also in this case constitutes electrostatic attractions.

In Figure 12.25(b), one example is given for measurements performed on the acid mixture from the North Sea crude. After addition of salt, the IFT shows a stair-formed progress until it equilibrates 10 to 15 units below the starting value. The stair-formed curve is most likely a result of a combination of two processes. Firstly, since the mixture is polydisperse, small molecules will reach the interface at an earlier stage than the larger ones due to higher diffusion rate. Gradually, however, the smallest molecules will be replaced by larger molecules as they cross the interface due to high water solubility. A stepwise adsorption of monomers to the interface might thus occur. Secondly, for polydisperse mixtures, more dynamic processes are taking place at the interface than for monodisperse surfactants and normally longer time is required to get the system equilibrated. The sequential drops in IFT might thus refer to temporary states before the real equilibrium is reached as the curves flatten out. At this final state, the interface is covered by a film comprising more interfacially active molecules in combination with the divalent cations.

### 12.3.5 Quartz Crystal Microbalance

The quartz crystal microbalance (QCM) has been known for several decades and a variety of devices are available. Common for all these instruments are that they utilize an electric field to oscillate a crystal, and find the resonance frequency. Adsorption of a compound increases the mass of the crystal and thereby lowers the resonance frequency. The principle is shown in Figure 12.26, and the lateral displacement is typically 1 to 2 nm [90]. The odd numbered harmonics can also be recorded, and in the case of a rigid and thin adsorbate, they will give the equivalent response as the fundamental frequency. As the overtones have smaller amplitude, they are changed more for the adsorbed mass close to the surface rather than a thick layer. Sauerbrey's equation [91] is used when the adsorbate is rigid (i.e., low dissipation values, described below) and a thin layer. Then the harmonic oscillations will give a linear relation between change in mass $\Delta m$ and change in resonance frequency $\Delta f$,

$$\Delta m = -\frac{\rho_q \cdot \upsilon_q \cdot \Delta f}{2 f_0^2 \cdot n} = -C\frac{\Delta f}{n} \tag{12.14}$$

Here $\rho_q$, $\upsilon_q$, and $f_0$ are the specific density, shear wave velocity, and fundamental resonance frequency, respectively, and are constant for each quartz crystal. The factor $n$ is one for the fundamental frequency, three for the third harmonic oscillation, five for the fifth harmonics, etc. Newer instruments also measure the dissipated energy, the inverse of the Q-factor.

$$D = \frac{1}{Q} = \frac{E_{Dissipated}}{2\pi E_{Stored}} \tag{12.15}$$

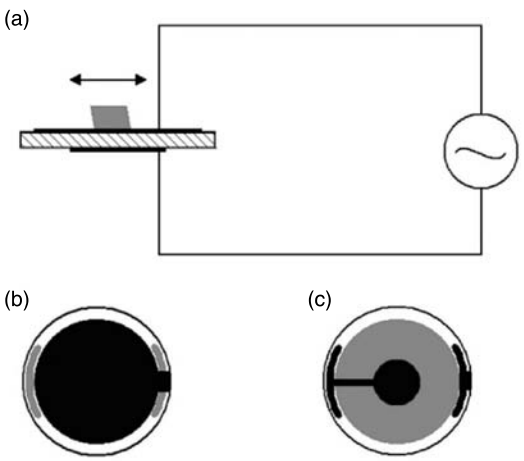


**FIGURE 12.26** The heart of the QCM is the AT-cut quartz crystal sandwiched between two gold electrodes. (a) The crystal is given a mechanical lateral oscillation by an oscillating potential difference, and its resonance frequency is dependent on the mass. (b) The larger gold electrode is facing the solution investigated, and the area where the adsorption is measured is slightly larger than (c) the smaller counter electrode. Crystals used in Q-sense and KSV instruments are 1.4 cm in diameter, has electrode thickness of 100 nm, 5 MHz resonance frequency, and the factor C in Sauerbrey's equation 17.7 ng $cm^{-2}$ $Hz^{-1}$.

The more viscous the adsorbed layer is the more energy is lost from the oscillation. Q-Sense QCM-D instrument measures the damping of the oscillation when the electrical circuit driving the oscillation is opened. KSV-Z500 uses impedance measurements to find the resonance frequencies and the Q-factor. Other QCM devices are made by Elchema, EG&G, Maxtek, and Universal.

The QCM technique is very sensitive, and measures data every second or even faster depending on the model. The sensitivity in liquid is 1 ng $cm^{-2}$ for adsorption, and a D value of $4 \times 10^{-8}$ compared to D value around $1 \times 10^{-6}$ in air (Q-Sense QCM-D). This makes it suitable for surfactant adsorption that traditionally is measured by depletion method.

One of the advantages with measuring adsorption with QCM is that crystals can be coated with different materials, and a variety of surfaces ($SiO_2$, stainless steels, polystyrene, titanium, and many metals) are available from suppliers. Thin metal oxide films, polymer coating, and organic films can be deposited with a spin coater, and compounds like cellulose can be deposited with the Langmuir–Blodgett technique.

#### 12.3.5.1 Applications

Corrosion inhibitors are usually investigated in corrosion experiments, using weight loss of coupons or electrochemical methods as a measure of their protecting properties. Little is known beyond that they adsorb to steel surfaces. We have used QCM to study adsorption processes of a corrosion inhibitor (quaternary ammonium) onto iron and cementite, mimicking the steel walls of a oil pipe [92]. From the kinetics it is seen that the adsorption and desorption is a fast process and that maximum adsorption is achieved around the critical micelle concentration. The adsorbed mass is less than what is needed for a monolayer/bilayer, hence it is likely that the adsorbed corrosion inhibitor organize on the surface like discrete aggregates. Varying the chain length of the quaternary ammonium, or adding salt to the system, changed the concentration for maximum adsorption. However, this is due to changing the critical micelle concentration. Corrosion inhibitors are often dissolved in alcohols when injected into oil pipes, therefore we also investigated the effect of alcohols on the adsorption. The typical solvent methyl ethylene glycol did not change the level of the adsorbed amount of quaternary ammonium. The effect of long chain alcohols was also investigated as they behave like cosurfactants and can alter the geometry of the adsorbate. At concentrations of 25 mM hexanol with quaternary ammonium, the QCM gave a sudden increase in adsorbed mass, corresponding to a bilayer. When the quaternary ammonium was removed from the bulk solution, the adsorbed mass slowly decreased, indicating a more stable adsorbate.

It is important that the surfactant is added in moderate concentrations in the QCM experiments to be certain that it does not change the viscosity and density of the bulk solution. The effect of carbon chain lengths on the adsorption of the model corrosion inhibitor (alkyltrimethylammonium bromide) on cementite is presented in Figure 12.27. The surfactant adsorption increases with concentration up to the critical micelle concentration. The long-chain homologues, with carbon chain $C_{14}$ and upwards, flatten out completely at this concentration, while the shorter compounds seem to give higher adsorption. As the CMC increases with the shorter carbon chain lengths, these observations are attributed to the bulk effect. Thus, there are two contributions to the change in frequency, the actual adsorption of mass, and the changes in the bulk solution. A comparative study of adsorption of nonionic surfactants on silica from benzene applying QCM and depletion methods has been reported [93]. Both methods agree very well for the series of poly (ethylene glycol) ethers at low concentrations. However, large deviation is observed for the nonyl phenol ethoxylate, and this is explained by the interactions between the benzene solvent and the phenyl in the adsorbed surfactant.

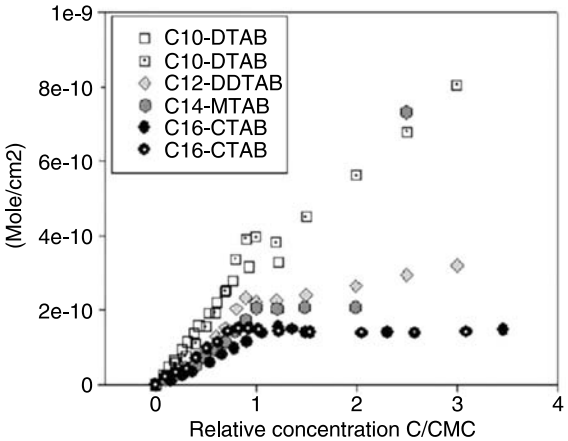


**FIGURE 12.27** Adsorption of the cationic surfactant alkyltrimethylammonium bromide on a cementite surface, measured with QCM. The concentration along the *x* axis is normalized with respect to the critical micelle concentration for the sake of comparison. As the shorter homologs have higher CMC, it is likely that the frequency change is due to both adsorption and the changed bulk properties. While the C16TAB flattens out at CMC, the C10TAB continues to increase.

Different solvents can be used in the QCM adsorption measurements, and unlike optical methods like ellipsometry, the solution does not need to be transparent. The adsorption of asphaltenes and resins from organic solutions has been investigated with this technique. As explained in previous sections, asphaltene precipitation may cause problems in the oil production chain, all the way from reservoir to refinery. The solvents and presence of indigenous oil-soluble surfactants like resins can affect the precipitation and adsorption to surfaces, and the phenomena has been investigated with the QCM method and a hydrophilic surface [94]. It was found that the adsorbed amount of resins from a heptane solution corresponds to a rigidly attached monolayer. The amount adsorbed decreased with an increasing amount of toluene and was virtually zero in pure toluene. Asphaltenes adsorb in large quantities and the mass and dissipation show that it is adsorbed as aggregates on the surface. The aggregates were firmly attached, and could not be removed by adding resins. The system of asphaltenes and resins in mixture was markedly different from the adsorption of the pure compounds as the compounds associate in the liquid bulk, and it was concluded that the preformed resin aggregate adsorbed to the surface.

The majority of QCM experiments have been carried out on biological systems, using gold or a modified surface. The effect of hydrophilic surfaces is that lipid vesicles can adsorb as monolayer, bilayer, or intact vesicles [95]. A close study of the adsorption on a silica surface [96], which gives the bilayer structure, is complemented by SPR and AFM studies, and together they give a complete picture of the process on silica surface. First, lipid vesicles are adsorbed, until a certain coverage where the vesicles collapse and a bilayer without any visible defects are formed. The adsorbed mass from SPR and QCM agrees well after the vesicle collapse on the surface, and the water inside the vesicles is released. The lipid vesicles and bilayer are a good starting point for further investigations of reactions. For example a fluid biotin containing phospholipid bilayer supported on an $SiO_2$ surface immobilized with the tetrameric protein streptavidin to give a rigid layer. Then a mixed sequence 15-mer biotin-PNA and DNA with identical base pair sequences were linked to streptavidin, and the difference in adsorption of fully complementary DNA was

detectable [97]. It was also possible to differentiate adsorption of complementary DNA and a singly mismatched DNA.

### 12.3.6 Atomic Force Microscopy

Atomic force microscopy (AFM), invented in 1986 [98], is a type of the scanning probe microscope, and measures the attracting/repulsive forces arising when two bodies are close to each other. The force is measured by using a cantilever with a certain spring constant (0.01 to 100 N $m^{-1}$) that is pulled towards the investigated surface in case of attraction, or pushed up in case of repulsion from the investigated surface. On the downside of the cantilever is a well defined tip (most often $Si_3N_4$ or Si), and on the reverse side is a reflective surface. The cantilever displacement is most often measured with the laser beam deflection method [99,100]. A laser beam is reflected from the rear side of the cantilever, and the cantilever displacement is detected as deflected beam hitting a split diode photodetector. A sketch of the main components in an AFM is given in Figure 12.28, and the typical deflection-distance curve in Figure 12.29. AFM is used for measuring force between two bodies approaching–retracting and for imaging of a surface by letting the probe scan the surface in the *xy* plane in contact, non-contact, and tapping mode. The strength of AFM lies in its extreme resolution and its operating conditions. At optimal conditions, large atoms on the surface can be seen in the images, such as graphite [101], mica [102], boron nitride [103], and NaCl (001) [104].

Various modulation techniques can be used when AFM experiments are carried out. *Force spectroscopy*, that is moving the cantilever in the *z* direction with no movement in the *xy* plane, is used for measuring different surface mechanical properties. The first direct measurements in air and water were using tips with complex or unknown geometry. With the development of the colloidal probe, where a microsphere is glued to the AFM tip, a better force measurement is possible. The spherical geometry allows a comparison with theoretical predictions. When the spring constant of the cantilever is known, the raw data from a force measurement can be

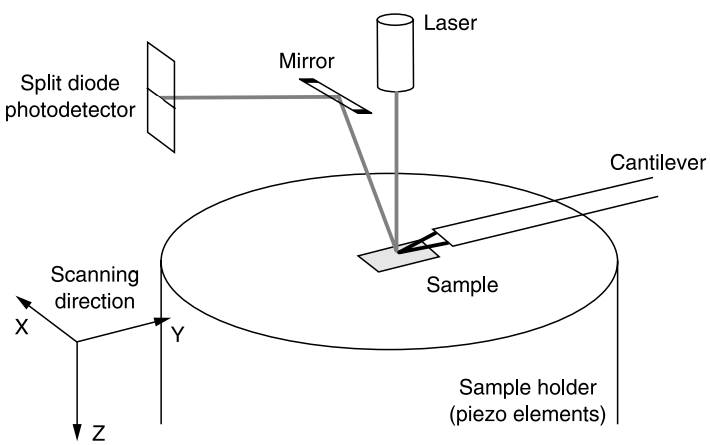


**FIGURE 12.28** AFM main components. The deflection of the cantilever changes the reflected laser beam which is detected by a split diode photodetector (divided in two or four parts). The sample holder is built around a cylindrical piezo element with several electrodes, which controls the *xy* movements used for scanning images and the *z*-direction for height control.

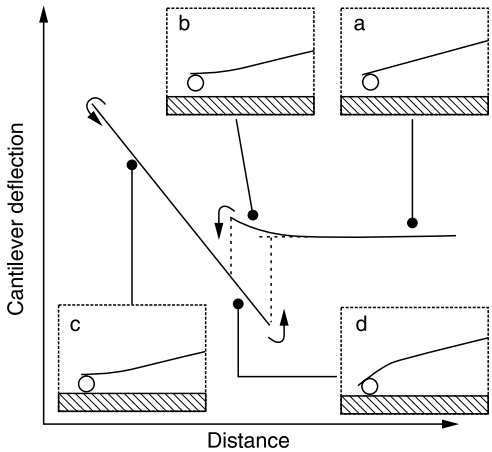


**FIGURE 12.29** A typical deflection–distance curve. (a) Far apart the cantilever is not interacting with the surface and the zero-line is obtained. (b) As the cantilever approaches the surface the cantilever is deflected by coulombic forces before the jump-to-contact, noted by the dotted line. (c) For hard surface a linear compression–decompression is observed with a slope proportional to the spring constant of the cantilever. (d) When the cantilever is withdrawn from the surface the adhesive forces will hold it in contact with the sample until jump-off-contact.

converted by using the method of Neumeister and Ducker [105] to a force versus tip separation curve. Forces that are measured with the AFM are capillary, Coulomb, van der Waals, double layer, solvation, hydration, hydrophobic specific, and steric forces [106]. The high sensitivity of soft cantilevers can measure forces at the pico-newton level and can be used to measure intermolecular forces, interactions between single molecules or single molecules and surfaces. In such experiments a single molecule is fixed to the cantilever tip with covalent bonding, and the force is measured as the cantilever rises.

In *contact mode* the probe is lowered until contact with the sample. Imaging takes place by scanning the surface in the *xy* plane, and the topography is given as the vertical displacement of the cantilever gives the *z* direction. A useful option in contact mode is the lateral force microscopy (LFM), or frictional force microscopy, that measures the lateral force on the tip causing buckling and torsion of the cantilever [105].

The *non-contact* mode was developed for surface imaging based on attractive forces rather than repulsion. The tip is lowered to the surface, but halted before jump-to-contact. A sharp AFM probe can easily cut through the aggregates and record images of the surface beneath if ordinary contact mode is used. The force experienced is the double layer repulsion between the tip and the sample.

In *tapping mode* the cantilever is made to oscillate by piezoelements on the cantilever or by acoustics when used in a liquid cell. The advantage of this mode is the absence of lateral torsional forces and reduced damage to the tip and the sample, and is suitable for imaging softer materials. The amplitude of the oscillating cantilever is damped when the tip is close enough to interact with the surface. A PID regulator regulates the *z* direction to keep amplitude constant through the scan.

In addition to the above techniques, *phase imaging* is a powerful imaging technique. It is based on the tapping mode and utilizes the phase lag between the periodic signal driving the

oscillation and actual oscillation of the cantilever. Images from phase shift give the contrasts due to surfaces with different hardness, hydrophilicity, magnetic fields, and other surface properties.

#### 12.3.6.1 Applications

Atomic force microscopy features many techniques of great interest in colloid and surface science. It has the great advantage over other techniques that it can work in gases and liquids, the natural environment for colloidal systems. Characteristic for colloidal particles is the extremely large surface area, and the interface reactions and attraction/repulsion of particles are therefore one of the main interests. The three different regions of a force–distance curve (contact line, non-contact region, and zero line) contain different information. In the contact region an elastic material will give a straight line with no hysteresis, while a plastic surface will not follow a retracting cantilever and therefore give loading–unloading hysteresis. There are different theories for the interpretation of the contact region. Hertz theory from 1881 [107] considers an elastic sphere on a flat surface and applies in some cases, but does not take into account neither surface forces or adhesion. The theory gives the reduced Young modulus expressed by the Young modulus and Poisson ratios of the sample and the tip. Sneddon's theory [108] considers the case when the indenter is not deformed while the surface takes the deformation. This gives an expression for the force exerted by the tip/sample contact and the deformation of the surface which is solved numerically. Three theories, Bradley, Derjaguin–Müller–Toporov, and Johnson–Kendall–Roberts, take into account the effect of surface energies on the deformation on the contact deformation. Maugis [109] has the most complete theory, which applies for materials ranging from large rigid spheres with high surface energies to small compliant bodies with low surface energies. Above the linear contact line in Figure 12.29 we find the non-contact region. This contains information about the repulsive and attractive forces between two bodies. The approach curve is increasing until the jump-to-contact is observed when the gradient of the tip–sample interactions exceeds the elastic constant of the spring. The maximum value of the attractive force is equal to the jump-to-contact cantilever deflection times the spring constant of the cantilever. Knowing the tip shape, it is possible to evaluate the force. The Hamaker constant can be calculated in two ways: (1) fitting one of the force laws to the attractive part of the force laws, or (2) to use the jump to contact force, and calculate it from the relation to van der Waals force and the geometry. In a review of force spectroscopy, Cappella and Dietler [106] have evaluated the Hamaker constants determined experimentally with theoretically derived values. They remark that the first measurements done did not take the capillary force into account, and give too high values. Measurements in water give significantly lower values, and even though the experimental error is large they often show a valid trend with surface energies. Upon withdrawal of the cantilever a jump-off-contact takes place when the cantilever spring constant is larger than the gradient of the tip–sample interaction. At this point the product of the cantilever deflection and the spring constant equals the adhesive forces. The jump-off-contact is related to the surface energies and geometry. The pull-off force gives many adhesive material properties, but is not an accurate method for determining the surface energies.

#### 12.3.6.2 Atomic Force Microscopy Imaging and Colloidal Systems

##### *12.3.6.2.1 Topography of a Substrate*

AFM imaging reveals the structure of adsorbate on solid surfaces. A surface that appears planar to the naked eye can still be rough on the micro- or nano scale. The imaging technique determines the surface rugosity/roughness in micro- and nano range.

#### 12.3.6.2.2 Adsorbate on a Surface

AFM can also be used for determining coverage and structure of an adsorbate on a surface, the adsorbate being a self-assembly structure, a Langmuir–Blodgett (L–B) film, biopolymers (proteins, DNA, cells, viruses etc.), and other substances. Most of the samples need to be imaged under water to eliminate the capillary forces. Mica is the most common substrate for adsorption on hydrophilic surfaces, as it has a well defined charge density and planar surface. Graphite is chosen for adsorption on hydrophobic surfaces.

Self-assembly structures are very soft, and therefore difficult to image. The non-contact AFM is suitable as the tip is not in contact with the surface. The first direct imaging of "hemimicelles," analogous to bulk micelle, was CTAB on graphite [110]. An overview of AFM imaging of cationic surfactants [111] shows the effect of counter-ion, carbon chain length, and cosurfactant on surfaces like mica and graphite.

The Langmuir–Blodgett technique is suitable for depositing water-insoluble compounds to a substrate, where the compound (e.g., lipids, particles, biopolymers) is packed on a water surface to a known surface pressure and area per unit. Then it is transferred to a solid surface by dipping a substrate into the solution with sufficiently low speed. It can be used to find structure and eventual defects. L–B films of cadmium arachidate on mica [112] show that the method is suitable for studying the quality of a deposited L–B film. The technique has also been used for investigating the effect of resins and asphaltene inhibitors on the precipitation of colloidal asphaltene [113]. In this study monolayers of asphaltenes and resins were transferred onto mica substrates using the L–B technique, and the topography analyzed by means of AFM.

This work shows the structural change in the monolayer when the composition of the film was gradually changed from pure asphaltenes to pure resins. Pictures of pure asphaltene show a closed-packed layer of round disks or rod formed units. Addition of resins will change this rigid structure towards a more open network with regions completely uncovered by film material. Pure resins build up a layer with an open structure, i.e., more like a fractal pattern.

Another observation is the growth of the size of the individual film units upon addition of resins. This indicates interactions between asphaltenes and resins, providing aggregates of larger dimensions than observed for the pure fractions. Small and moderate amounts of resins give rise to a more polydisperse distribution of the film material, while a further increase in the resin content (i.e., 60 wt% resins) reduces the polydispersity, i.e., the monolayer becomes more uniform in component size when one of the pure fractions dominates the film properties.

AFM pictures of asphaltene films containing 100 ppm of different high molecular weight demulsifiers/inhibitors were also investigated and it was demonstrated that these components introduce similar effect on the film as the structural changes initiated by the resins. These results indicate that the observed changes in the film, i.e., opening of the structure and increased size of the film components, are qualitatively essential in order to reduce the emulsion stability.

AFM images of samples of supported planar lipid-protein membranes and actin filaments have been obtained by applying a very low force to the cantilever [114].

Biomaterial is often dissolved into a very dilute aqueous solution and either sprayed on mica in a small amount, or a droplet is left on for a while before the excess is blown off with an inert gas. In some cases pretreatment of the mica, or counter-ion in the solution, is necessary to get sufficient bonding to the surface; for instance mica is soaked in magnesium acetate 2 h and rinsed with water prior to DNA (aq) addition [115]. Another method of fixing material to the surface is to use molecules with thiol or silane groups that bind to the surface and another group that binds to the desired particle. Determining particle size distribution of nano-particles is possible if no aggregation takes place and being aware of the convolution of the image. Convolution of

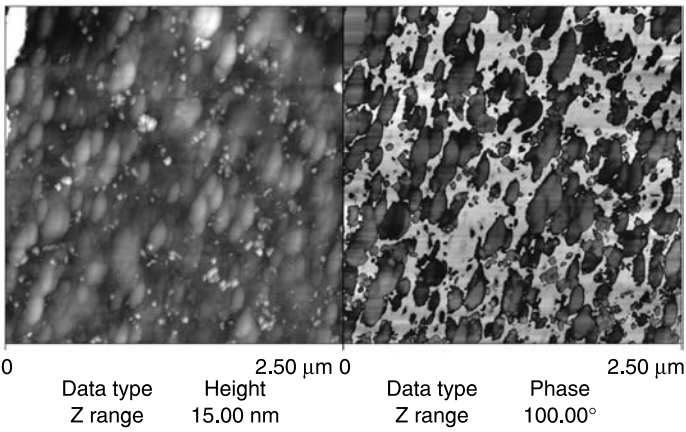


**FIGURE 12.30** AFM image of an iron surface exposed to solution of sodium oleate and poly-DADMAC. The topography (left) only give the structure of the sputtered iron, and the thin film of organic material is not visible. The phase image (right) shows that the iron (dark region) is partly covered with a softer organic material (bright region).

an image will make particles larger as the tip on the cantilever has a certain size. Dealing with very small particles, the width in the image is larger than the true dimension. Determining size of nano-particles of Pd, Au, CdS, and ZnS based on the height is in good agreement with TEM with an average of ~3 nm, while the radius in the *xy* plane is about 50 nm [116]. The same was observed earlier [117] for particles of 37 ± 5 nm (TEM) to be 95 ± 12 nm in AFM.

Contrast between different regions can be enhanced with phase imaging. It is often a much more sensitive measurement technique than the amplitude detection. The phase shift is due to variations in composition, adhesion, friction, viscoelasticity, and electric and magnetic properties. The phase imaging is not only getting better contrast. It can get out information that is not visible in the topography image at all. Figure 12.30 shows the topography image and the simultaneously recorded phase image of a surfactant and polymer adsorbed on an iron surface. The two regions with different hardness are distinguishable in the image to the right. Tapping on iron gives little phase shift, while the tapping of surfactant and polyelectrolyte gives a significant phase shift, and appears as bright regions. In wood pulp fibers the technique can be used to show how the lignin component is distributed on the cellulose surface. Phase imaging can also be used to visualize the distribution of hard particles in a softer matrix, like in composite materials [118,119], or different crystalline phases in polymers.

### 12.3.7 Plasmachemical Surface Modification

The plasma state can be defined as a gaseous mixture of freely moving charged particles which overall are electrically neutral. More specifically, the plasma is a blend of electrons, ions, molecular fragments, radicals, excited states, photons, and neutral atoms and molecules. The degree of ionization in the plasma depends highly on how the plasma is generated. Here the focus will be on so-called cold discharges. These are low-pressure, non-equilibrium plasmas where the degree of ionization typically is less than 10%, and direct current (DC), radio frequency (RF), or microwave (MW) power sources are used to generate and maintain the plasma.

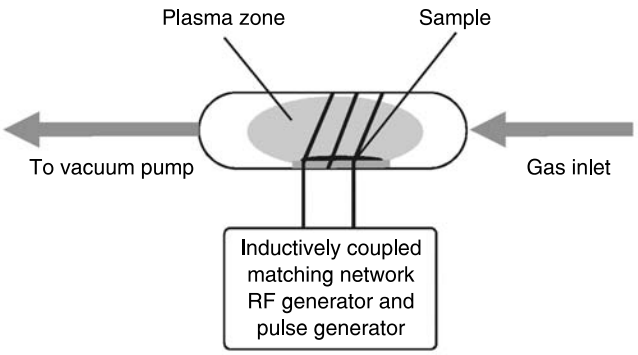


**FIGURE 12.31** A plasma chamber.

The schematic set-up of an inductively coupled RF plasma chamber is shown in Figure 12.31. The main parts are the glass chamber where the samples are placed, the inlet for gas or vapor on one side and the outlet to a vacuum pump, via a nitrogen cold trap, on the other side. A copper coil is wound around the glass chamber, and connected to a 13.56 MHz RF generator, via a matching network. The purpose of the matching network is to match the output impedance from the RF generator with the impedance in the chamber. A pulse generator can also be connected to the RF generator if pulsed plasmas are desired.

When a sample is placed in the chamber and a steady state, low-pressure flow is obtained through the system, the RF generator and matching network is turned on in order to create an electrical field. A plasma state is then generated by acceleration of free electrons in the electromagnetic field, and the kinetic energy of these will reach a level where ionization, excitation, and molecular fragmentation will occur. Since the electron mass is much smaller than the mass of molecular and atomic species, the kinetic energy of the electrons is high compared to the ions and free radicals (i.e., the plasma is not in equilibrium). Typical energies of the electrons are between 0.5 and 5 eV, and this is intense enough to dissociate chemical bonds and form radicals in most organic structures. Interactions between the sample and plasma species will then entail plasmachemical modification of the sample surface. The non-equilibrium energy distribution in the plasma enables chemical reactions to proceed via nonthermodynamic channels at approximately room temperature, while a corresponding thermally activated reaction could require temperatures as high as 10,000 °C.

The most important variables in the system described here are the power into the chamber, the pressure in the chamber prior to ignition of the plasma, and the time the sample are exposed to the plasma state. Furthermore, the type of surface modification the samples undergo depends on the properties of the gas or vapor going into the chamber. In polymerizing plasmas, molecular fragmentation leads to reorganization of species and formation of macromolecular structures, so-called plasma polymers, which will deposit as thin films on the sample. Properties such as film thickness and functional groups can be controlled by the experimental variables. In nonpolymerizing plasmas fragmentation and implantation of functional groups occur directly.

Etching occurs in plasma systems with high particle energies, and since material is removed from the sample surface, the process is typically used for cleaning of surfaces. Finally, plasma activated grafting is a two-step process where an inert plasma is used to activate the substrate, and subsequently a reactive vapor is led above the sample in order to modify the surface.

#### 12.3.7.1 Applications

Much research has been carried out on plasmachemical modification of flat substrates [120], but very little has been done on particles. However, a study of how the level of amine loading on porous polymer beads is affected by the physical properties of the particles has been carried out by Øye et al. [121–124]. A range of highly cross-linked polystyrene beads with different particle sizes and pore structures were modified by allylamine plasma. Allylamine is polymerizing in the plasma state, and the external surface of all the particle types were readily covered by a thin film. Raman spectroscopy chemical mapping and scanning electron microscopy of cross-sectioned beads revealed that the smallest beads (15 μm in diameter) had a uniform distribution of amine groups throughout the particles. However, partial filling of the pore structure by the plasma polymer was also observed. For larger beads, there was an accumulation of amine groups towards the outer edge of the particles. The effective penetration of the plasma polymer was found to be 3 to 4 μm, and also in this case it partially filled the pores. An alternative functionalization method was tried out in order to reduce the pore filling effects. This entailed activation of the porous polymer beads by inert argon plasma, and subsequent grafting by diaminopropane. In this case a more homogenous amine distribution was obtained for larger beads as well.

The ultimate goal was to utilize the plasma modified particles in solid-phase synthesis of organic compounds, and several synthesis schemes were carried out. Generally, it was found that the low available amine loading of the modified beads, in comparison with commercial beads, resulted in limited amounts of recovered material. However, the produced yields were comparable to those obtained for commercial bead systems. Furthermore, a scavenging process using benzoyl chloride as a model electrophile was carried out. These processes are normally fast, and the fastest rate was obtained for the plasma enhanced diaminopropane grafted beads. The allyl amine modified material gave slower scavenging rates, also compared to a commercial material.

Plasmachemical modification by water plasma has also been used to surface oxidize carbon nanofibers (CNFs) [125]. CNFs have attracted large interest for use as catalyst supports. The surface chemistry is essential for this application, as oxygen moieties on the surface will improve the fiber–metal precursor interactions during impregnation or deposition precipitation of the materials. It was shown that in this study that the ratio between acidic and basic oxygen surface sites could be tailored by varying the conditions in the plasma chamber.

### 12.3.8 Contact Angles

The primary focus of contact angle studies is in assessing the wetting characteristics of solid/liquid interactions. A sessile drop of liquid on a solid surface will be affected by two kinds of forces, namely gravity forces and surface forces. In most cases, the gravity forces can be neglected for small droplets and the behavior is determined by surface forces.

Contact angle is a quantitative measure of the wetting of the solid by the liquid. The less the contact angle, the higher is the degree of wetting. If it is greater than 90° it is said to be nonwetting. On the other hand, a contact angle of zero represents complete wetting.

A correlation between contact angle and surface forces, given in terms of the interfacial tensions between the involving phases, may be given by the Young equation:

$$\gamma_{sg} = \gamma_{sl} + \gamma_{lg} \cos\theta \tag{12.16}$$

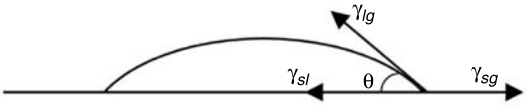


**FIGURE 12.32** A sketch of a sessile drop, showing the contact angle $\theta$ and the vectors of interfacial tensions between the various phases.

Here, $\gamma_{sg}$, $\gamma_{sl}$, and $\gamma_{lg}$ are the interfacial tensions between solid–gas, solid–liquid, and liquid–gas, respectively, whereas $\theta$ is the contact angle (Figure 12.32). The corresponding spreading coefficient is defined according to:

$$S = \gamma_{sg} - (\gamma_{sl} + \gamma_{lg}) \tag{12.17}$$

Contact angle is commonly used as the most direct measure of wetting. Other experimental parameters, like work of adhesion, work of cohesion, work of spreading, and wetting tension, may be derived directly from contact angle and surface tension results. A detailed theoretical review of the theory of contact angle is given by Good [126].

Several experimental techniques are today available for contact angle measurements [127]. The CAM 200 equipment is based on goniometry, one of the most traditional techniques for solid–liquid systems. In conventional goniometry the contact angle can be assessed directly by measuring the angle formed between the solid and the tangent to the drop surface. Consequently, the assignment of the tangent line is the limited factor in reproducibility, and significant errors might occur, especially if the instrument is operated by multiple users.

For CAM 200 this potential problem is avoided by utilizing computer analysis of the drop shape to generate consistent contact angle data. The Young–Laplace equation (equation 12.10) is then fitted to the drop profile and the tangent might be assigned in the intersection between the curve and the baseline.

### 12.3.9 Zeta Potential

Surface charges will arise when particles are suspended in a solution. The most common ways these occur is by ionization of chemical groups on the surface, differential loss of ions from the crystal lattice, or by adsorption of charged species from the surrounding solution. The presence of ions in the liquid will also be influenced by the surface charges, as the concentration of counter-ions will increase close to the charged solid–liquid interface. The consequence of this is that an electrical double layer is built up around the particles [128]. This layer is commonly divided into an inner layer, the so-called Stern layer, where the ions are adsorbed onto the charged particle surface and a diffuse layer, often called the Gouy–Chapman layer, containing more loosely bound ions. Factors that will affect the thickness of the electrical double layer are pH, ion strength, and concentration of additives such as surfactants. Furthermore, when particles move, by diffusion or in a gravitational or induced field, a shear plane exists outside which the ions in the double layer will no longer be influenced by the movements of the particles. The potential at this boundary is defined as the zeta potential, and several experimental techniques can be used to measure it. Electro-osmosis, streaming potential, and sedimentation potential are treated in more detail elsewhere, while the focus in the following will be on electrophoresis.

The result of applying an electrical field across a suspension of charged colloidal particles is that the particles move towards the oppositely charged electrode. The constant velocity that

is obtained in the electric field with equilibrium with the opposing viscous forces is called the electrophoretic mobility. The zeta potential and the electrophoretic mobility are linked by the Henry equation:

$$u_E = \frac{2\varepsilon\zeta f(\kappa a)}{3\eta} \tag{12.18}$$

where

$u_E$ = electrophoretic mobility
$\varepsilon$ = dielectric constant of the solvent
$\zeta$ = zeta potential
$f(\kappa a)$ = Henry's function
$\eta$ = viscosity of solvent

Henry's function is effectively the ratio of the particle radius to the electrical double layer thickness, as $\kappa$ and $a$ represent the thickness of the electrical double layer and the radius of particles, respectively. For large values of $\kappa a$, Henry's function approaches 1.5. This is called the Smoluchowski approximation, and the relation between the zeta potential and electrophoretic mobility is straightforward within this limit, i.e., when the particles are much larger than the double layer thickness. Henry's function approaches 1 for small values of $\kappa a$, and this is the Hückel approximation. Also, in this case, the relationship between the zeta potential and electrophoretic mobility is very simple, and the particles are much smaller than the double layer thickness. Both these approximations are normally available in instruments used for measuring the electrophoretic mobility.

In the Malvern Zetasizer system the electrophoretic mobility is measured by laser Doppler velocimetry (LDV). In this method a He–Ne laser at 633 nm is first split, and subsequently made to cross in the capillary cell containing the sample. Young's interference fringes of known spacing are created at the crossing point. As the particles move through this pattern by an applied electric field, the scattered light undergoes similar fluctuations, and the frequency of fluctuations is related to the velocity of the particles. The scattered light is collected by an avalanche photodiode and the signals transferred to a digital correlator. Analysis of the correlation function (described in detail in the following section) gives a frequency spectrum that is utilized to calculate the electrophoretic mobility and subsequently the zeta potential.

#### 12.3.9.1 Applications

The film properties of reservoir particles were described in the Langmuir section. Figure 12.33 shows the zeta potential as a function of pH for the same particles. The hydrophilic Type II particles have a negative zeta potential over the entire pH range, while the Type I particles have an isoelectric point at pH 6.84. The difference is due to adsorbed species on the Type I particles.

The zeta potential as a function of pH was also measured for plasma oxidized carbon nanofibers [125]. It was found that the ratio between acidic and basic surface groups was dependent on the power of the water plasma. Furthermore, zeta potential has been used to study the electrokinetic properties of oil-in-water emulsions [129] and dispersed asphaltenes [130,131].

### 12.3.10 Dynamic Light Scattering

Dynamic light scattering (DLS) is a means of measuring particle size and particle size distribution of dilute suspensions in the range from ~2 nm to ~2 μm. For particles in this size range, the only

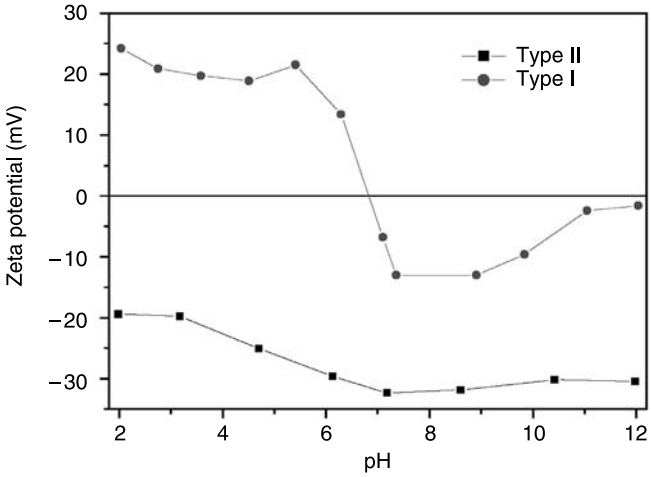


**FIGURE 12.33** Zeta potential of reservoir particles.

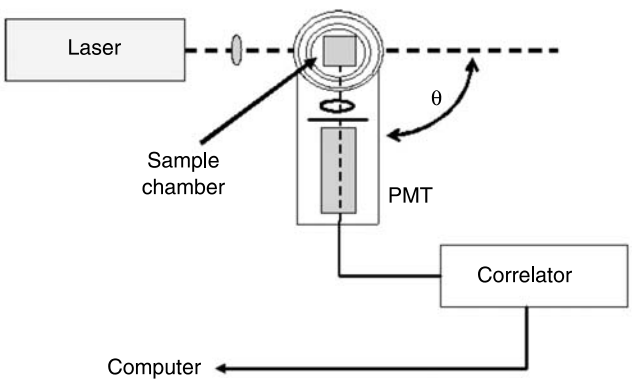


**FIGURE 12.34** Instrumental set-up for a DLS experiment. The scattered light is collected at an angle $\theta$ (usually 90°), before passing through a photomultiplier tube (PMT) to the computer.

major competing technique is electron microscopy. However, electron microscopy experiments are often slow, sample preparation can be tedious, and it is only cost- and time effective to measure a small amount of sample, leading to poor statistics and the risk of not displaying a representative part of the sample. DLS has the advantage of being rapid, of requiring little or no sample preparation, and of having a solid statistical foundation through measuring a large number of particles per experiment.

In dynamic light scattering, a laser beam (usually a He–Ne laser, $\lambda$ = 633 nm) is utilized to probe a small volume of particle suspension, as shown in Figure 12.34.

As the particles undergo Brownian motion, interference between scattered light produces a time-dependent intensity fluctuation at the detector, where the intensity i(s,t) fluctuates around an

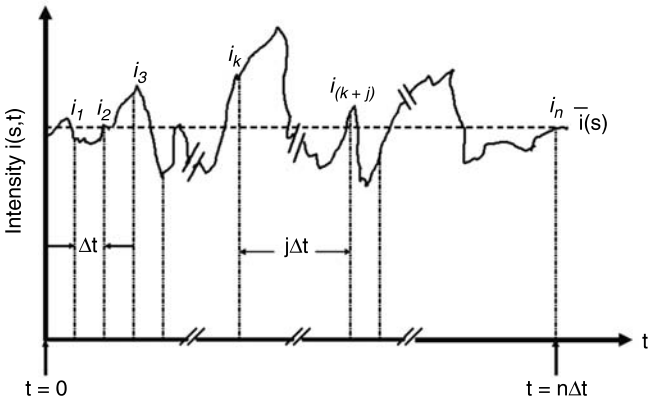


**FIGURE 12.35** Schematic illustration of the intensity of scattered light with time (From Hiemenz PC, Rajagopalan R. *Principles of Colloid and Surface Chemistry*; 3rd ed.; Marcel Dekker, Inc: New York, 1997. [201].)

average value $\bar{i}(s)$ as illustrated in Figure 12.35.

$$\bar{i}(s) = \lim_{t_n \to \infty} \frac{1}{t_n} \int_0^{t_n} i(s,t)dt \approx \lim_{n \to \infty} \sum_{j=1}^{n} i(s, j\Delta t) \tag{12.19}$$

where j is the number of discrete time intervals $\Delta t$, and s is the scattering vector, a function of the laser output wavelength $\lambda$ and the angle of the detector relative to the incident beam $\theta$:

$$\begin{aligned} s &= \frac{4\pi}{\lambda} \sin\left(\frac{\theta}{2}\right) \xrightarrow[\lambda=633\ l\text{nm}]{\theta=\pi/2} s \\ &= \frac{4\pi}{633\text{nm}} \sin\left(\frac{\pi}{4}\right) \end{aligned} \tag{12.20}$$

This temporal fluctuation is then modeled as the decay between its highest value $\overline{[i(s,0)]^2}$ and its lowest asymptotic value $\left[\bar{i}(s)\right]^2$ as a function of delay time $t_d$ between measurements to yield the autocorrelation function $C(s,t_d)$ as shown in Figure 12.36 [132,133]:

$$\begin{aligned} C(s,t_d) &= \lim_{t_n \to \infty} \int_0^{t_n} i(s,t)i(s,t+t_d)dt \\ &= \overline{i(s,0)i(s,t_d)} \\ &\approx \lim_{n \to \infty} \sum_{k=0}^{n} i(s,k\Delta t)i(s,(k+j)\,\Delta t) \end{aligned} \tag{12.21}$$

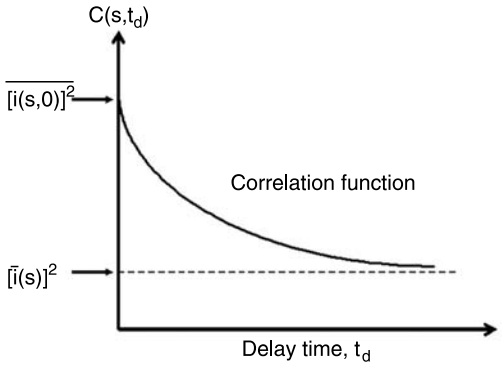


**FIGURE 12.36** Schematic illustration of the variation of the autocorrelation $C(s,t_d)$ with delay time $t_d$. (From Hiemenz PC, Rajagopalan R. *Principles of Colloid and Surface Chemistry*; 3rd ed.; Marcel Dekker, Inc: New York, 1997.)

By applying the Siegert relation, the ratio of the autocorrelation function $C(s,t_d)$ to its asymptotic value $\left[\bar{i}\,(s)\right]^2$ can be found:

$$\frac{C(s,t_d)}{\left[\bar{i}(s)\right]^2} = g_2(s,t_d) = 1 + \xi\,|g_1(s,t_d)|^2 \tag{12.22}$$

where $\xi$ is an instrumental constant approximately equal to unity.

For a dilute suspension of (non-interacting) monodisperse spherical particles, $g_1(s,t_d)$ reduces to:

$$g_1(s,t_d) = e^{-s^2 D t_d} \tag{12.23}$$

where D is the self-diffusion coefficient of the particle, and s is the magnitude of the scattering vector as defined above. Application of the Stokes–Einstein equation yields the hydrodynamic particle radius $R_H$ (see Figure 12.37) from the diffusion coefficient:

$$D = \frac{kT}{6\pi\eta R_H} \tag{12.24}$$

where $\eta$ is the viscosity of the suspending fluid.

In polydisperse systems, the overall decay of $g_1(s,t_d)$ is determined by the decay rate $s^2D$ corresponding to each particle size, and can be written as a weighted average of all possible decays:

$$g_1(s,t_d) = \lim_{n\to\infty} \sum_{j=1}^{n} w_j \left(s^2 D\right) e^{-s^2 D_j t_d} \tag{12.25}$$

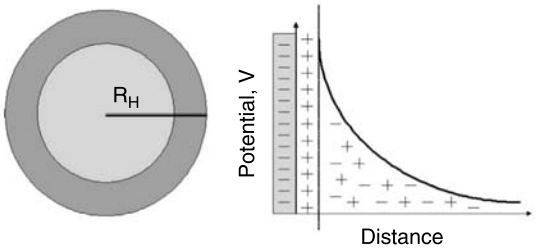


**FIGURE 12.37** Illustration of the hydrodynamic radius $R_H$ of a spherical particle with an overall negative surface charge.

where $w_j(s^2D)$ is a weighting function determined by the population in size range j. As real systems rarely, if ever, are truly monodisperse, numerical algorithms such as cumulant expansion (Z-average) [134], CONTIN [135,136], NNLS [137,138] etc. are required in order to properly fit Equation 12.25. What algorithm to use depends on what prior knowledge exists of the system to be studied, and on what model best fits the data set (yields the highest correlation coefficient).

#### 12.3.10.1 Applications

In addition to its routine application in studies of polymers [139,140], food emulsions [141], and drug delivery vectors [142], dynamic light scattering has been widely used for studying coagulation rates in colloidal systems [143–147], including aqueous suspensions of gold nanoparticles. Wilcoxon and co-workers have studied the aggregation behavior – kinetics and structure – of gold sols with respect to addition of functional ligands (such as dyes), changes in pH, and addition of salt [147]. Here, the large scattering cross section of gold colloids enables detection of low concentrations, but the strong extinctions may also lead to distortion of the relaxation time, thus making accurate particle size measurements difficult, a problem which is compounded by the aggregation process. Dynamic light scattering has also been used for determination of Ostwald ripening rates and destabilization phenomena in aqueous emulsions [143]. Furthermore, aggregation and precipitation of asphaltenes have been studied by this technique [148–151].

### 12.3.11 UV–Visible Spectroscopy

The recent interest in nanotechnology has spurred resurgence in the use of steady-state absorption and emission spectroscopy in colloid and surface chemistry. In contrast to the corresponding bulk materials, material properties in the colloidal domain, including optical, are size-dependent. Metal colloids such as gold and silver nanoparticles and quantum dots exhibit strongly size-dependent extinctions in the visible frequency spectrum. This allows for observation of the flocculation behavior of the sol by monitoring the absorption bands of the system. Moreover, it is possible to look at changes in the dielectric function on the gold surface from adsorption of chromophores and emitters, as will be described later in this section.

Figure 12.38 shows a simple two-state diagram which represents the three processes considered in a quantum mechanical treatment of the radiation field: (stimulated) absorption, stimulated emission, and spontaneous emission, represented by the phenomenological rate constants $B_{12}$, $B_{21}$, and $A_{21}$, respectively.

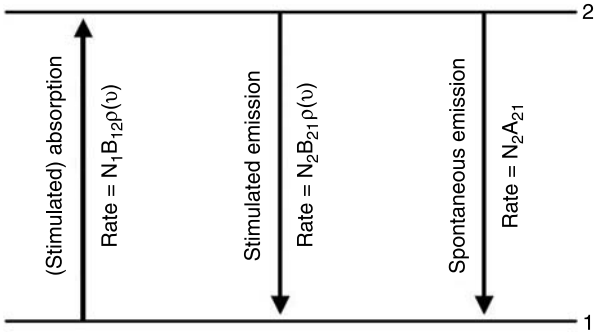


**FIGURE 12.38** Einstein coefficients for absorption and emission.

The rate of transitions out of a state is proportional to the population (number of molecules) in that state. Designating the populations of the lower and upper levels by $N_1$ and $N_2$ and letting $\rho(\nu)$ represent the frequency dependent energy density of the radiation, the rates of upward ($W_{12}$) and downward ($W_{21}$) transitions can be expressed as follows:

$$W_{12} = N_1 B_{12} \rho(\nu) \tag{12.26}$$

$$W_{21} = N_2 B_{21} \rho(\nu) + N_2 A_{21} \tag{12.27}$$

To maintain equilibrium, the rates of upward and downward transitions must be balanced:

$$N_1 B_{12} \rho(\nu) = N_2 B_{21} \rho(\nu) + N_2 A_{21} \tag{12.28}$$

In linear spectroscopy experiments, the Boltzmann populations of the two states are unperturbed [152]:

$$\frac{N_2}{N_1} = \frac{g_2}{g_1} \exp\left[\frac{-(E_2 - E_1)}{kT}\right] = \frac{g_2}{g_1} \exp\left[\frac{-h\nu}{kT}\right] \tag{12.29}$$

Here, the possibility of degeneracy is allowed for; $g_i$ is the number of states at the energy level $E_i$. Assuming that the energy density is that of a black body:

$$\rho(\nu) = \frac{8\pi h \nu^3}{c^3} \frac{1}{e^{h\nu/kT} - 1} \tag{12.30}$$

Combining Equations 12.28, 12.29, and 12.30 and solving for the energy density gives the relationships between the Einstein coefficients:

$$g_1 B_{12} = g_2 B_{21} \tag{12.31}$$

$$\frac{A_{21}}{B_{21}} = \frac{8\pi \nu^3}{c^3} \tag{12.32}$$

Although Equation 12.32 demonstrates the frequency dependency of the ratio of the rate constants for spontaneous to stimulated, $A_{21}$ and $B_{21}$ are not directly comparable as they are not

dimensionally equivalent. Thus, a better comparison is of the rates $A_{21}$ with $B_{21}\rho(\nu)$, the ratio of which is $A_{21}/B_{21}\rho(\nu) = e^{h\nu/kT} - 1$. It is clear from this ratio that when $h\nu \gg kT$, as is usually the case for luminescence experiments, the rate of spontaneous emission greatly exceeds that of stimulated emission. Thus, in systems at equilibrium at room temperature, the spontaneous emission of light at optical frequencies is greatly favored over stimulated emission. The properties of the two types of radiation are quite different; in the case of stimulated emission, the stimulated photon has the same properties as the incident radiation, resulting in emission which is collimated and coherent, whereas spontaneous emission, such as ordinary fluorescence, is emitted in all directions with random phase, and is red-shifted as compared to the incident radiation.

Although many principles presented thus far are quite general, the focus of this section is on applications in electronic spectroscopy or, more specifically, UV–vis absorption. The intensity of absorption by a sample varies with the path length x of the sample in accord with Beer–Lambert's law [153]:

$$\log\frac{I}{I_0} = -\varepsilon Cx \tag{12.33}$$

where $I_0$ is the incident intensity at a particular wavelength, I is the intensity after passage through a sample of length x (in cm), and C is the molar concentration (in mol/L) of the absorbing species. The quantity $\varepsilon$ (or $\varepsilon(\nu)$) is called the molar absorptivity (formerly, and still widely, referred to as the extinction coefficient), and is generally expressed in L $mol^{-1}$ $cm^{-1}$. The dimensionless product $A = \varepsilon Cx$ is called the absorbance of the sample, and the ratio $I/I_0$ is the transmittance T. These two quantities are related as follows:

$$\log T = -A \tag{12.34}$$

Hence, the absorbance is indirectly measured experimentally by determining the ratio of the incident to emerging intensities and applying Equation 12.34.

Information gathered from UV–vis absorption is not necessarily limited to information about the concentration and frequency of electronic transitions of a molecule or solid. By applying the Fermi Golden Rule (FGR) transition rate for (stimulated) absorption

$$B_{if} = \frac{|\mu_{if}|^2}{6\varepsilon_0\hbar^2} \tag{12.35}$$

between two states i and f, where $\mu_{if}$ is the transition dipole moment between the ground (i) and first excited (f) electronic states respectively, it is even possible to find the absolute value of the given transition moment through use of the integrated molar absorptivity [152]:

$$|\mu_{if}|^2 = \frac{\left(6\varepsilon_0\hbar^2\right)2303c}{N_A hn}\int_{band}\frac{\varepsilon(\nu)}{\nu}d\nu \tag{12.36}$$

where n is the refractive index of the medium, $N_A$ is Avogadro's number, and the integer 2303 is a conversion factor.

The intensity of emission $f \rightarrow i$ is also proportional to $|\mu_{if}|^2$ and to $A_{fi}$, although there are several reasons why this is not a practical way to determine the radiative lifetime (to be discussed in the next section) or the transition dipole moment. One reason is that fluorescence intensities, unlike absorption intensities, are difficult to quantify, due to the emitted radiation being spread

in all directions with random phase. The signal observed will depend strongly on the angle subtended by the detector, so it is sensitive to experimental conditions. One does not usually have the advantage of being able to compare a sample and a reference beam as in absorption spectroscopy.

#### 12.3.11.1 Applications

It is well known that the optical signature of gold nanoparticles is strongly dependent on particle size and interparticle distance [154,155]. Thus, by monitoring the position and full width at half maximum (FWHM) of the plasmon band, information about the stability and flocculation behavior of the suspension can be collected. When the interparticular distance is substantially greater than the average particle diameter, the nanoparticle suspension appears red, but as the interparticle distance decreases to less than approximately the average particle diameter, the color shifts to blue or purple, depending on the level of flocculation and the particle concentration. The changes in peak position and in FWHM of the plasmon band as observed in UV–visible spectroscopy have been used to obtain experimental conditions where surface modification of the gold nanoparticles do not induce aggregation on the time scale of the experiment [156], to determine the critical coagulation concentration of gold nanoparticles capped with various stabilizing agents [157], and to monitor photoinduced fusion of gold colloids [158,159]. Moreover, the changes in optical signature have been widely used in colorimetric detection schemes for DNA-linked gold nanoparticle assemblies [160–167]. Here, the color changes from red to blue/purple accompanying changes in the flocculation behavior has been utilized to detect and monitor the programming of assemblies of two- and three-dimensional architectures, and to detect and quantify hybridization of gold nanoparticle-immobilized oligonucleotides. Figure 12.39 illustrates the principle behind the programmed materials synthesis of DNA-linked gold nanoparticle assemblies. The strong visible extinctions of gold nanoparticles have also been used for characterizing the presence, location, and properties of gold nanoparticles dispersed in mesoporous solids [168–173]. *In situ* synthesis of gold nanoparticles within ordered mesoporous materials can be monitored with UV–visible spectroscopy, as shown in Figure 12.40. The presence of a plasmon band indicates the presence

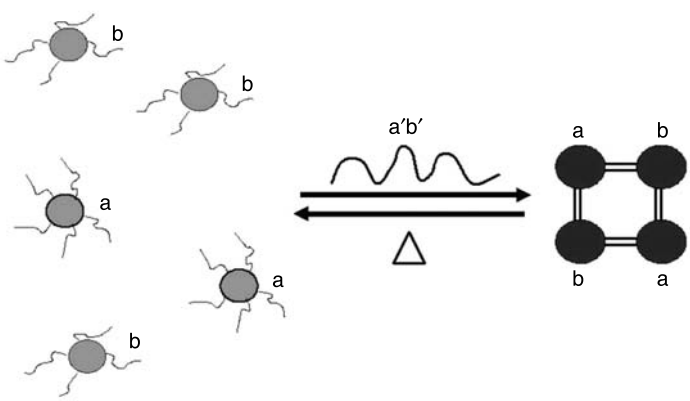


**FIGURE 12.39** Programmed materials synthesis and accompanying changes in optical signature of DNA-capped gold nanoparticles. Two probe species (a and b) are linked by a complementary DNA target strand (a′b′).

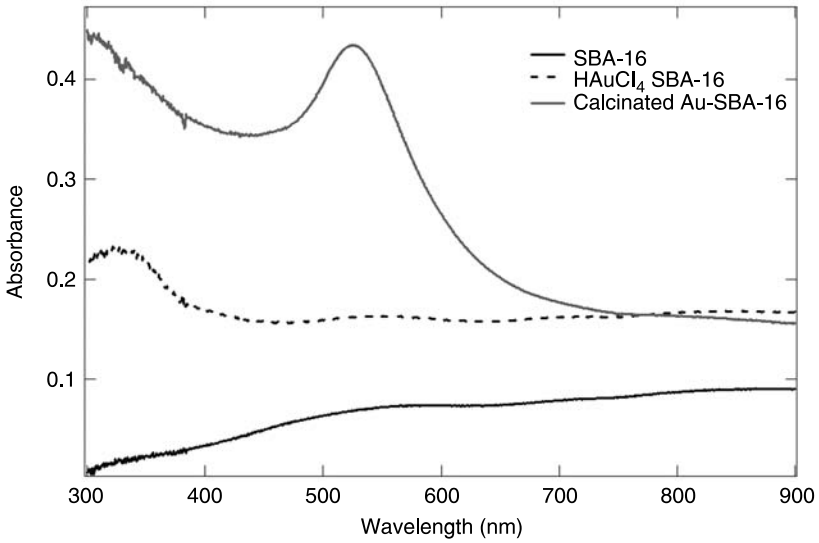


**FIGURE 12.40** UV–visible spectrum of gold nanoparticles synthesized within the ordered mesoporous material SBA-16. When only the gold nanoparticle precursor ($HAuCl_4$) is present, no plasmon band is observed in the material. Following thermal reduction, a distinct absorption band centered at ~520 nm appears – the gold nanoparticle plasmon band.

of gold nanoparticles with a diameter ≥3 nm [174]. Shifts in the peak position of the plasmon band can be attributed to changes in the dielectric function on the gold nanoparticle surface. Thus, changes in the spectral lineshape of gold nanoparticles yield information about the chemical environment of the colloids. Shifts in the peak position of the plasmon band $\lambda_{max}$ towards lower frequencies (red shifts) have been attributed to interfacial charge transfer reactions between the nanoparticles and the pore walls for gold nanoparticles dispersed in mesoporous materials [171]. Conversely, shifts in the $\lambda_{max}$ towards higher frequencies (blue shifts) of gold [175] and silver [176] nanoparticles dispersed on porous supports have been ascribed to coherent coupling of the plasmon resonances of closely spaced colloidal entities. This coupling would be facilitated by gold (or silver) nanoparticles residing within the pore system of the ordered mesoporous material rather than on the external surface.

UV–visible spectroscopy can also be used for the study of changes in the dielectric function on the nanoparticle surface as a result of adsorption of dyes and chromophores and emitters on noble metal colloids [156,177]. Franzen and co-workers have studied the optical properties of dye molecules adsorbed on single gold and silver nanoparticles, using different particle sizes, solvent conditions, and passivating layers [156]. The dye molecules were similar to those reported in studies of surface-enhanced Raman scattering (SERS). From the observed spectral changes of the adsorbates, the dyes studied could be divided into two classes according to the nature of the interaction between the adsorbate (dye) and the substrate (gold or silver nanoparticles), and the position of the absorption band of the dye relative to the plasmon frequency $\omega_p$ of the nanoparticles (see Figure 12.41). Dyes where the absorption band occurred at higher frequencies than the plasmon frequency, and where the adsorption to the nanoparticles most likely involved chemical bonding, showed little or no changes in the absorption spectrum following adsorption.

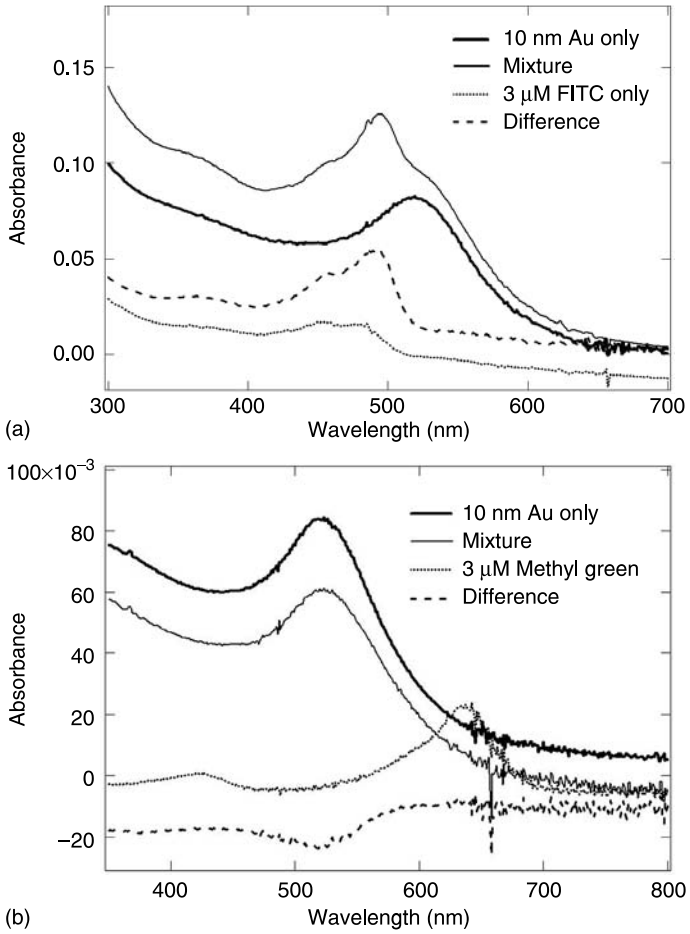


**FIGURE 12.41** UV–visible spectra of Class I (a) and Class II (b) adsorbates. (a) Illustration of Class I adsorbate behavior. UV–visible spectra of F5ITC (5 μM) adsorbed to 10 nm citrate stabilized Au nanoparticles in a 50/50 $H_2O$/MeOH solvent. (b) Illustration of Class II adsorbate behavior. UV–visible spectrum of methyl green (3 μM) adsorbed to 10 nm citrate stabilized Au nanoparticles in a 50/50 $H_2O$/MeOH solvent. The difference spectra were obtained by subtracting the nanoparticle-only spectrum from the spectrum of the adsorbate–nanoparticle mix.

This set of dyes was denoted Class I adsorbates. However, dyes with absorption bands occurring at lower frequencies than $\omega_p$, and where the adsorption most likely occurred through electrostatic interactions, showed significant bleaching of the absorption spectrum following adsorption. This set of adsorbates was denoted Class II. As the changes in the optical signature of the adsorbates depend on the size, surface charge, and nature of the nanoparticles, this effect could be called colloidochromism. This is illustrated in Figure 12.41(a), where the absorbance spectrum of a pH sensitive Class I adsorbate, fluorescein-5-isothiocyanate (F5ITC), is enhanced by a factor of ~5. This enhancement can be ascribed to either (1) a change in the pKa of the dye upon adsorption due to the interaction with the dielectric function on the gold surface or (2) a response to the local pH on colloidal gold surfaces being different to the solution pH.

### 12.3.12 Time-Correlated Single Photon Counting Spectroscopy

Emission experiments are typically performed in sample geometries that are large relative to the size of the emitters and relative to the absorption and emission wavelengths. In this arrangement, the emitters radiate into free space [178]. These free-space conditions serve as the basis for our knowledge and intuition about emission, i.e., fluorescence and phosphorescence. However, the presence of nearby metallic surfaces, defined as highly conducting particles of a surface and not metal ions or oxides, can alter the free-space condition, the result of which could be dramatic spectral changes as compared to those observable in the absence of metal surfaces. These changes are due to interactions of the excited-state emitters with free electrons in the metal, which polarize the metal and impose a reactive field on the emitter [179–183], the observable effect of which is an alteration of the radiative decay rates and thus the observed lifetimes of the excited state of an emitter. This observable effect is usually referred to as "quenching," as the presence of a metal surface often provides additional nonradiative pathways for the emitter [184–188], thus altering the measured lifetime of the excited state $\tau_{obs}$. Time-resolved spectroscopies such as TCSPC make it possible to do direct measurements of the excited-state lifetimes of emitters.

Under free-space conditions, the quantum yield $F_{rad}$, as well as the observed lifetime of the excited/radiative state $\tau_{obs}$, of an emitter are determined by the rates of radiative decay, $k_{rad}$, and nonradiative decay, $k_{nr}$, to the ground state. The quantum yield is defined as [152]:

$$\Phi_{rad} = \frac{k_{rad}}{k_{rad}+k_{nr}} = \frac{k_{rad}}{k_{obs}} \tag{12.37}$$

The observed lifetime in the absence of metallic surfaces is given by:

$$\tau_{obs} = (k_{rad} + k_{nr})^{-1} = (k_{obs})^{-1} \tag{12.38}$$

The natural lifetime [189] of the radiative excited state of an emitter ($\tau_N$) is the inverse of the radiative decay rate ($\tau_N = k_{rad}^{-1}$), which is the lifetime if $k_{nr} = 0$ or $F_{rad} = 1$.

When the emitter is associated with a quencher, i.e., a metallic surface such as a nanoparticle, an additional nonradiative process with a rate $Q = k_q[Qu]$ is introduced, which competes with emission. Here, $k_q$ represents the rate constant for the quenching process, and [Qu] represents the concentration of the quencher. The quantum yield $\Phi_{rad,Q}$ and observed lifetime $\tau_{obs,Q}$ are now given by:

$$\Phi_{rad,Q} = \frac{k_{rad}}{k_{rad} + k_{nr} + Q} = \frac{k_{rad}}{k_{obs,Q}} \tag{12.39}$$

$$\tau_{obs,Q} = (k_{rad} + k_{nr} + Q)^{-1} = \left(k_{obs,Q}\right)^{-1} \tag{12.40}$$

For mixed systems, such as a suspension of a quencher (like gold colloids) with an emitter (i.e., a fluorophore-labeled protein, peptide, or other macromolecule) where the concentration of emitter exceeds the number of adsorption sites on the quencher, the total decay rate $k_{tot}$ as measured by TCSPC can be resolved into two components: (1) a decay rate representing the fraction of emitter associated with the quencher $k_{obs,Q}$, and (2) a decay rate representing the fraction of emitter under free-space conditions (not associated with the quencher) $k_{obs}$ as given by Equations 12.39 and 12.37, respectively, where the corresponding lifetimes are given by Equations 12.40 and 12.38. In order to separate these time components and quantify the

concentrations of quenched and free emitter, the measured decay $k_{tot}$ can be normalized and fitted to a sum of exponentials so as to maximize the correlation coefficient of the fit, $R^2$:

$$Y(t) = \sum_{i=1}^{N} A_i e^{-k_i t} \tag{12.41}$$

where N is the total number of luminescent components, and $A_i$ and $k_i$ represent the amplitude/fraction/population and rate constant for each component, respectively. The decay rates are identified as either quenched ($k_{obs,Q}$) or free ($k_{obs}$) by comparison with the decay rate in a sample containing only free emitter. For systems obeying Stern–Volmer type quenching, $k_{obs,Q} \gg k_{obs}$, and thus $\tau_{obs,Q} \ll \tau_{obs}$. The concentrations of quenched and free emitter can now be determined by multiplying the total emitter concentration by the appropriate amplitude/fraction $A_i$ associated with each decay rate/lifetime. By comparing the concentration of surface-bound emitter with the concentration of quencher, i.e., Au nanoparticle, the ratio of emitter (or labeled macromolecule) to quencher can be determined.

#### 12.3.12.1 Applications

One application for time-correlated single photon counting spectroscopy has been studies of energy migration dynamics in light-harvesting antenna polymer systems derivatized with Ru(II) and Os(II) polypyridyl complexes [190–192]. For mixed Ru(II) and Os(II) systems, efficient energy transfer is expected to occur, based on the high degree of overlap between the emission spectrum of the donor – Ru(II)* complexes – and the absorption spectrum of the acceptor – Os(II) complexes. Because the Os(II) excited state lies 0.36 eV below the Ru(II) excited state, the Os sites are considered to be deep traps that terminate the energy migration process [190,191]. In the development of molecular assemblies for studies in energy conversion, an important issue is the coupling of light absorption to electron transfer indirectly by use of intervening energy transfer in an antenna array. Another critical factor in the development of these nanoscale assemblies is the ability to control the spatial arrangement of the molecular components, especially if intermolecular energy-transfer and charge-transfer processes are at the core of the material's function. Spatial organization can be achieved through the design of covalently bonded supramolecules in which molecular subunits are linked together so that their relative geometries (i.e., separations and orientations) are well defined [193–198]. Derivatized polymers are attractive choices for positioning of molecular constituents because they offer flexibility and simplicity in the design of multicomponent assemblies. The functional capabilities of light/harvesting systems can be quantified on the basis of the efficiency with which they conduct excited-state energy. For efficient conduction to occur, the time scale for energy transfer must be fast compared to the lifetime of the excited state. For example, if the time scale for an excited state to hop to an adjacent site is 10 times faster than its lifetime $\tau_N$, energy transfer will occur with 90% efficiency. Thus, efficient energy transfer is best achieved by combining fast energy transfer between monomer units with long-lived excited states.

The Papanikolas group has studied the photophysical properties of Ru(II) and Os(II) polypyridyl complexes linked to polystyrene through use of TCSPC and steady-state spectroscopies, and by Monte Carlo simulations [190,191]. A series of supramolecular assemblies consisting of 20 Ru(II) and/or Os(II) polypyridyl coordination complexes with varying Ru(II)/Os(II) ratios linked together through a polystyrene backbone as shown in Figure 12.42 were synthesized and investigated. Here, the Ru(II) complexes can act as efficient "antennas" for collecting visible light and sensitizing the lower energy Os(II) sites on the polymeric backbone. Energy transfer

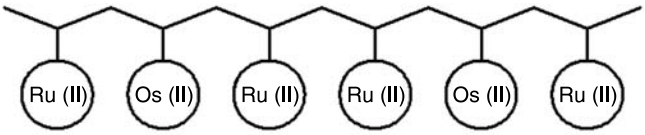


**FIGURE 12.42** Illustration of the Ru(II)/Os(II) complexes linked together through a polymer backbone.

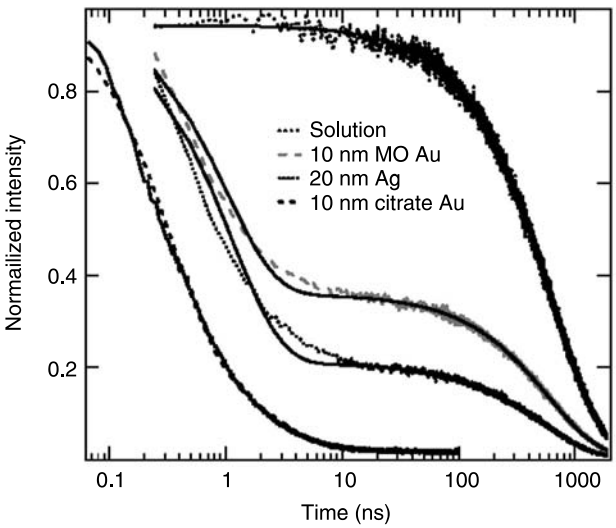


**FIGURE 12.43** Time-resolved normalized emission from $Ru(bpy)_3^{2+}$ in solution and adsorbed onto various colloids, including 10 nm mercaptooctanoate (MO) stabilized Au colloids ($3.1 \times 10^{-9}$ M), 20 nm citate stabilized Ag colloids, and 10 nm citrate stabilized Au colloids ($4.7 \times 10^{-9}$ M). The solution concentration of $Ru(bpy)_3^{2+}$ was kept at $\sim 6 \times 10^{-6}$ M. The excitation wavelength was 423 nm, and emission was detected at 630 nm. Experimental data is shown as a dashed or dotted line, and the fit is shown as a solid line.

efficiency was found to be dependent on the degree of Os(II) loading, however; with an average loading of 11 Ru(II) sites per 5 Os(II) sites, the energy transfer Ru(II)* $\rightarrow$ Os(II) was determined to occur with an efficiency of 95% independent of excitation wavelength from 420 to 500 nm.

Glomm et al. [177] have described the application of Ru(II) tris bipyridine ($Ru(bpy)_3^{2+}$) and Os(II) tris bipyridine ($Os(bpy)_3^{2+}$) as phosphorescent labels for the quantification of surface binding of molecules to gold and silver nanoparticles. The fraction of $Ru(bpy)_3^{2+}$ and $Os(bpy)_3^{2+}$ in solution can be distinguished from the surface-confined fraction by the relative lifetimes and integrated emission yields as determined by TCSPC. Complementary steady-state measurements confirmed surface attachment of the phosphorescent label molecules. Figure 12.43 shows the time-resolved normalized emission from $Ru(bpy)_3^{2+}$ in solution and adsorbed onto gold and silver colloids. Here, it is evident that the observed emission traces for mixed $Ru(bpy)_3^{2+}$ and metal colloid systems consists of two or more decay rates, where at least one of the excited states has a significantly shorter lifetime than that of $Ru(bpy)_3^{2+}$ free in solution (Figure 12.43). In other words, the traces of mixed $Ru(bpy)_3^{2+}$ and metal colloid systems contain one component

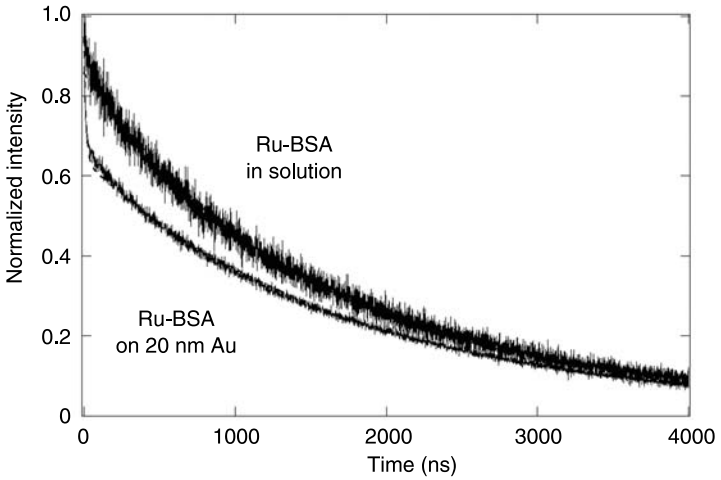


**FIGURE 12.44** Normalized intensity versus time for $[Ru(bpy)_2bpy\text{-}C_6H_{12}\text{-}S]^{2+}$-BSA (Ru-BSA) in solution and adsorbed onto 20 nm gold colloids. The concentration of Ru-BSA was $2 \times 10^{-7}$ M, and the 20 nm Au colloid concentration was $4 \times 10^{-10}$ M. Data are shown as dashed lines, and the fits are shown as solid lines.

with a lifetime corresponding to that of $Ru(bpy)_3^{2+}$ free in solution, and at least one component corresponding to quenched or surface-confined $Ru(bpy)_3^{2+}$. The amount of adsorbed luminescent molecules can then be quantified as shown in Equation 12.41.

In order for this technique to have a general applicability, it must be not only able to detect and quantify surface attachment of the label molecules themselves (i.e., $Ru(bpy)_3^{2+}$); it must also be able to distinguish between adsorbed and free states of bigger constructs, such as fluorophore-labeled proteins, peptides, and other macromolecules. However, it is important to note that when using constructs wherein luminescent labels are incorporated, the emission quantum yield of the construct will differ from that of the luminescent label molecule by itself. This technique has been proven effective for detecting and quantifying adsorption of Rhodamine-B labeled adenoviral receptor-mediated endocytosis (RME) peptide (CKKKKKKSEDEYPYVPN) on 5 nm and 20 nm gold colloids [199]. Further scale-ups of the technique have enabled quantification of Ru(bpy) labeled bovine serum albumin (BSA) adsorbed on gold nanoparticles [157,199]. For a 20 nm gold nanoparticle, monolayer coverage of BSA was determined to be $160 \pm 8$ protein molecules (see Figure 12.44). Multifunctional gold nanoparticle–peptide complexes where BSA functions partly as a stabilizer for the gold nanoparticles, and partly as a scaffold for covalent attachment of RME and nuclear localization signal (NLS) peptides to the gold–protein bioconstructs for use in targeted drug delivery, have been extensively studied by the Franzen and Feldheim research groups [142,157,199,200]. In order to preserve the functionality of the functional and targeting ligands, as well as to quantify the efficacy of the delivery vector in a given chemical and/or biological environment such as a specific cell line, detailed information about the interaction between each active component (proteins, peptides, oligonucleotides) with the substrate, such as obtained through use of TCSPC, is absolutely crucial.

TCSPC provides a rapid and powerful tool for direct measurement and quantification of surface-confined molecules [157,177,199]. Compared to steady state emission measurements, TCSPC has the advantage that one can distinguish a component that contributes only a few

percent to the total emission signal using the lifetime of that component. While steady-state emission measurements require the preparation of a series of samples with varying quencher concentrations and a reference in order to obtain Stern–Volmer plots, the method described here only requires a single sample plus a reference.

## ACKNOWLEDGMENTS

In preparing this chapter the authors would like to acknowledge the support of the industrial members of the Ugelstad Laboratory at NTNU in Trondheim. In addition we would also like to acknowledge The Research Council of Norway (NFR) for financial support to instrumentation and PhD candidates.

## REFERENCES

1. Speight, J. G. *The Chemistry and Technology of Petroleum*; 3rd ed.; Marcel Dekker, Inc.: New York, 1998.
2. Ali, M. A.; Nofal, W. A. *Fuel Science & Technology International* **1994**, *12*, 21–33.
3. Fan, T. G.; Buckley, J. S. *Energy & Fuels* **2002**, *16*, 1571–1575.
4. Hammami, A.; Ferworn, K. A.; Nighswander, J. A.; Overa, S.; Stange, E. *Petroleum Science and Technology* **1998**, *16*, 227–249.
5. Radke, M.; Willsch, H.; Welte, D. H. *Analytical Chemistry* **1980**, *52*, 406–411.
6. Suatoni, J. C.; Swab, R. E. *Journal of Chromatographic Science* **1976**, *14*, 535–537.
7. Hannisdal, A.; Hemmingsen, P. V.; Sjöblom, J. *Industrial & Engineering Chemistry Research* **2005**, *44*, 1349–1357.
8. Snyder, L. R.; Kirkland, J. J.; Glajch, J. L. *Practical HPLC Method Development*; 2nd ed.; John Wiley and Sons, Inc.: New York, 1997.
9. The Institute of Petroleum Standards Method, IP 469/01.
10. ASTM Standard 2001, D2007-01a.
11. Fan, T.; Buckley, J. S. *Energy Fuels* **2002**, *16*, 1571–1575.
12. Bharati, S.; Røstum, G. A.; Løberg, R. *Org Geochem* **1994**, *22*, 835–862.
13. Bharati, S.; Patience, R.; Mills, N.; Hanesand, T. *Org Geochem* **1997**, *26*, 49–57.
14. Mullins, O. C. *Analytical Chemistry* **1990**, *62*, 508–514.
15. Mullins, O. C.; Joshi, N. B.; Groenzin, H.; Daigle, T.; Crowell, C.; Joseph, M. T.; Jamaluddin, A. *Applied Spectroscopy* **2000**, *54*, 624–629.
16. Aske, N.; Kallevik, H.; Sjöblom, J. *Energy & Fuels* **2001**, *15*, 1304–1312.
17. Fossen, M.; Hemmingsen, P. V.; Sjöblom, J. *Journal of Dispersion Science and Technology* **2005**, *26*, 227–241.
18. Hildebrand, J. H.; Scott, R. L. *The Solubility of Nonelectrolytes*; 3rd ed.; Reinhold Publishing Corporation: New York, 1950.
19. Hansen, C. M. *Journal of Paint Technology* **1967**, *39*, 104–117.
20. Hansen, C. M. *Journal of Paint Technology* **1967**, *39*, 505–510.
21. Hansen, C. M. *Journal of Paint Technology* **1967**, *39*, 511–514.
22. Aske, N.; Kallevik, H.; Sjöblom, J. *Journal of Petroleum Science and Engineering* **2002**, *36*, 1–17.
23. Donaggio, F.; Correra, S.; Lockhart, T. P. *Petroleum Science and Technology* **2001**, *19*, 129–142.
24. Oh, K.; Ring, T. A.; Deo, M. D. *Journal of Colloid Interface Science* **2004**, *271*, 212–219.
25. Rogel, E.; León, O.; Espidel, Y.; González, Y. *Society of Petroleum Engineers Production & Facilities* **2001**, SPE no. 72050.
26. Rogel, E.; León, O.; Contreras, E.; Carbognani, L.; Torres, G.; Espidel, Y.; Zambrano, A. *Energy & Fuels* **2003**, *17*, 1583–1590.
27. Hu, Y. F.; Guo, T. M. *Fluid Phase Equilibria* **2001**, *192*, 13–25.
28. Aske, N.; Kallevik, H.; Johnsen, E. E.; Sjöblom, J. *Energy & Fuels* **2002**, *16*, 1287–1295.

29. Auflem, I. H.; Havre, T. E.; Sjöblom, J. *Colloid and Polymer Science* **2002**, *280*, 695–700.
30. McLean, J. D.; Kilpatrick, P. K. *Journal of Colloid and Interface Science* **1997**, *196*, 23–34.
31. McLean, J. D.; Kilpatrick, P. K. *Journal of Colloid and Interface Science* **1997**, *189*, 242–253.
32. Hemmingsen, P. V.; Li, X.; Peytavy, J. L.; Sjöblom, J. *Journal of Dispersion Science and Technology*, Submitted.
33. Chen, T. Y.; Mohammed, R. A.; Bailey, A. I.; Luckham, P. F.; Taylor, S. E. *Colloids Surf.* **1994**, *83*, 273–284.
34. Williams, T. J.; Bailey, A. G. *IEEE Trans. Ind. Appl.* **1986**, *IA-22*, 536–541.
35. Atten, P. *J. Electrostatics* **1993**, *30*, 259–270.
36. Førdedal, H.; University of Bergen: Norway, 1995.
37. Eow, J. S.; Ghadiri, M.; Sharif, A. O.; Williams, T. J. *Chem. Eng. J* **2001**, *84*, 173–192.
38. Eow, J. S.; Ghadiri, M. *Chem. Eng. J* **2002**, *85*, 357.
39. Kallevik, H.; Kvalheim, O. M.; Sjöblom, J. *J. Colloid Interface Sci.* **2000**, *225*, 494.
40. Aske, N.; Orr, R.; Sjöblom, J.; Kallevik, H.; Oye, G. *Journal of Dispersion Science and Technology* **2004**, *25*, 263–275.
41. Hemmingsen, P. V.; Silset, A.; Hannisdal, A.; Sjöblom, J. *Journal of Dispersion Science and Technology* **2005**, *26*, 615–627.
42. Havre, T. E.; Sjöblom, J. *Coll. Surf. A. Physiochem. Eng. Asp.* **2003**, *228*, 131–142.
43. Spiecker, P. M.; Gawrys, K. L.; Trail, C. B.; Kilpatrick, P. K. *Colloids Surfaces A* **2003**, *220*, 9–27.
44. Myrvold, R.; Hansen, F. K. *Journal of Colloid and Interface Science* **1998**, *207*, 97–105.
45. Wang, Y. Y.; Zhang, L.; Sun, T. L.; Jiayong, Y. *Journal of Colloid and Interface Science* **2004**, *270*, 163–170.
46. West, R. C.; Astle, M. J., Eds. *CRC Handbook of Chemistry and Physics*; 63 ed.; CRC Press, Inc.: Boca Raton, Florida, 1984.
47. Petty, M. C.; Barlow, W. A. In *Langmuir–Blodgett Films*; Roberts, G., Ed.; Plenum Press: New York, 1990, p 93.
48. Gaines Jr., G. L. *Insoluble Monolayers at Liquid–Gas Interfaces*; Wiley: New York, 1966.
49. Birdi, K. S. *Lipid and Biopolymer Monolayers at Liquid Interfaces*; Plenum Press: New York, 1989.
50. Harkins, W. D. *The Physical Chemistry of Surface Films*; Reinhold Publishing Corporation: New York, 1952.
51. Adam, N. K. *Physics and Chemistry of Surfaces*; 3rd ed.; Oxford University Press: London, 1941.
52. Smith, R. D.; Berg, J. C. *Journal of Colloid and Interface Science* **1980**, *74*, 273–286.
53. Pezron, E.; Claesson, P. M.; Berg, J. M.; Vollhardt, D. *Journal of Colloid and Interface Science* **1990**, *138*, 245–254.
54. Tomoaiacotisel, M.; Zsako, J.; Chifu, E.; Cadenhead, D. A. *Langmuir* **1990**, *6*, 191–197.
55. Honig, E. P.; Hengst, J. H. T.; Denengel, D. *Journal of Colloid and Interface Science* **1973**, *45*, 92–102.
56. Ese, M. H.; Yang, X.; Sjöblom, J. *Colloid and Polymer Science* **1998**, *276*, 800–809.
57. Singh, B. P.; Pandey, B. P. *Indian Journal of Technology* **1991**, *29*, 443–447.
58. Ese, M. H.; Galet, L.; Clausse, D.; Sjöblom, J. *Journal of Colloid and Interface Science* **1999**, *220*, 293–301.
59. Ese, M. H.; Selsbak, C. M.; Hannisdal, A.; Sjöblom, J. *J. Dispersion Sci. Technol.* **2005**, *26*, 145–154.
60. Ambwani, D. S.; Fort, T., Jr. *Surface and Colloid Science* **1979**, *11*, 93–119.
61. Stauffer, C. E. *Journal of Physical Chemistry* **1965**, *69*(*6*), 1933–1938.
62. Andreas, J. M.; Hauser, E. A.; Tucker, W. B. *Journal of Physical Chemistry* **1938**, *42*, 1001–1019.
63. Rotenberg, Y.; Boruvka, L.; Neumann, A. W. *Journal of Colloid and Interface Science* **1983**, *93*, 169–183.
64. Boucher, E. A.; Evans, M. J. B.; Jones, T. G. J. *Advances in Colloid and Interface Science* **1987**, *27*(*1–2*), 43–79.
65. Brandal, Ø.; Sjöblom, J.; Øye, G. *Journal of Dispersion and Science Technology* **2004**, *25(3)*, 367–374.
66. Brandal, Ø.; Hanneseth, A-M.; Sjöblom, J. *Colloid and Polymer Science* **2005** (Accepted).

67. Brient, J. A.; Wessner, P. J.; Doyle, M. N. In *Encyclopedia of Chemical Technology*; 4th ed.; Kirk-Othmer, Ed.; John Wiley & Sons: New York, 1995; Vol. 16, pp 1017–1029.
68. Seifert, W. K. *Fortschritte der Chemie Organischer Naturstoffe* **1975**, *32*, 1–49.
69. Tomczyk, N. A.; Winans, R. E.; Shinn, J. H.; Robinson, R. C. *10.1021/ef0201228* **2001**, *15*, 1498–1504.
70. Fan, T.-P. *10.1021/ef0201228* **1991**, *5*, 371–375.
71. Koike, L.; Reboucas, L. M. C.; Reis, F. d. A.; Marsaioli, A. J.; Richnow, H. H.; Michaelis, W. *Org Geochem* **1992**, *18*, 851–860.
72. Ovalles, C.; Carcia, M. d. C.; Lujano, D.; Aular, W.; Barmúdez, R.; Cotte, E. *Fuel* **1998**, *77*, 121–126.
73. Márquez, M. L. In *AICHE Spring National Meeting, Session T6005*: Houston, Texas, 1999; Vol. 99sp 56d.
74. Pathak, A. K.; Kumar, T. In *Proceedings of PETROTECH-95, Technology Trends in Oil Industry*: New Dehli, 1995, pp 217–224.
75. Poggesi, G.; Hurtevent, C.; Buchart, D. In *SPE Oilfield Scale Symposium*: Aberdeen, UK, 2002; Vol. SPE74649, pp 1–6.
76. Gallup, D. L.; Smith, P. C.; Chipponeri, J.; Abuyazid, A.; Mulyono, D. In *SPE International Conference on Health, Safety and Environment in Oil and Gas Exploration and Production*: Kuala Lumpur, Malaysia, 2002; Vol. SPE73960, pp 1–16.
77. Vindstad, J. E.; Bye, A. S.; Grande, K. V.; Hustad, B. M.; Hustvedt, E.; Nergård, B. In *5th SPE Oilfield Scale Symposium*: Aberdeen, UK, 2003; Vol. SPE80375.
78. Dyer, S. J.; Graham, G. M.; Heriot-Watt, C. A. In *5th SPE International Symposium on Oilfield Scale*: Aberdeen, UK, 2003; Vol. SPE 80395.
79. Havre, T. E. *Colloid and Polymer Science* **2004**, *282(3)*, 270–279.
80. Hartridge, H.; Peters, R. A. *Proc R Soc A* **1922**, *101*, 348–367.
81. Danielli, J. F. *Proc R Soc A* **1937**, *122*, 155–174.
82. Chifu, E.; Salajan, M.; Demeter-Vodnar, I.; Tomoaia-Cotisel, M. *Revue Roumaine de Chimie* **1987**, *32*, 683–691.
83. Rudin, J.; Wasan, D. T. *Colloids Surf* **1992**, *68*, 67–79.
84. Cratin, P. D. *J Dispersion Sci Technol* **1993**, *14*, 559–602.
85. Wolstenholme, G. A.; Schulman, J. H. *Trans. Faraday Soc.* **1950**, *46*, 475–487.
86. Goddard, E. D. *Journal of Colloid and Interface Science* **1967**, *24*(*3*), 297–309.
87. Veale, G.; Peterson, I. R. *Journal of Colloid and Interface Science* **1985**, *103*(*1*), 178–189.
88. Yazdanian, M.; Yu, H.; Zografi, G.; Kim, M. W. *Langmuir* **1992**, *8*, 630–636.
89. Avila, L. V. N.; Saraiva, S. M.; Oliveira, J. F. *Colloids and Surfaces, A: Physicochemical and Engineering Aspects* **1999**, *154*(*1–2*), 209–217.
90. Marx, K. A. *Biomacromolecules* **2003**, *4*, 1099–1120.
91. Sauerbrey, G. *Zeitschrift fuer Physik* **1959** *155*, 206–222.
92. Knag, M.; Sjöblom, J.; Øye, G.; Gulbrandsen, E. *Colloids and Surfaces A* **2004**, *250*, 269–278.
93. Caruso, F.; Rinia, H. A.; Furlong, D. N. *Langmuir* **1996**, *12*, 2145–2152.
94. Ekholm, P.; Blomberg, E.; Claesson, P.; Auflem, I. H.; Sjöblom, J.; Kornfeldt, A. *Journal of Colloid and Interface Science* **2002**, *247*, 342–350.
95. Keller, C. A.; Kasemo, B. *Biophys. J.* **1998**, *75*, 1397–1402.
96. Keller, C. A.; Glasmastar, K.; Zhdanov, V. P.; Kasemo, B. *Physical Review Letters* **2000**, *84*, 5443–5446.
97. Hook, F.; Ray, A.; Norden, B.; Kasemo, B. *Langmuir* **2001**, *17*, 8305–8312.
98. Binnig, G.; Quate, C. F.; Gerber, C. *Physical Review Letters* **1986**, *56*, 930–933.
99. Meyer, G.; Amer, N. M. *Applied Physics Letters* **1988**, *53*, 1045–1047.
100. Alexander, S.; Hellemans, L.; Marti, O.; Schneir, J.; Elings, V.; Hansma, P. K.; Longmire, M.; Gurley, J. *J. Appl. Phys.* **1989**, *65*, 164–167.
101. Binnig, G.; Gerber, C.; Stoll, E.; Albrecht, T. R.; Quate, C. F. *Europhysics Letters* **1987**, *3*, 1281–1286.
102. Drake, B.; Prater, C. B.; Weisenhorn, A. L.; Gould, S. A. C.; Albrecht, T. R.; Quate, C. F.; Cannell, D. S.; Hansma, H. G.; Hansma, P. K. *Science* **1989**, *243*, 1586–1589.

103. Albrecht, T. R.; Quate, C. F. *J. Appl. Phys.* **1987**, *62*, 2599–2602.
104. Meyer, G.; Amer, N. M. *Applied Physics Letters* **1990**, *56*, 2100–2101.
105. Neumeister, J. M.; Ducker, W. A. *Rev. Sci. Instrum.* **1994**, *65*, 2527–2531.
106. Cappella, B.; Dietler, G. *Surface Science Reports* **1999**, *34*, 1.
107. Hertz, H.; Reine, J. *Angew. Math.* **1881**, *92*, 156.
108. Sneddon, J. N. *Int. J. Eng. Sci.* **1965**, *3*, 47.
109. Maugis, D. *Journal of Colloid and Interface Science* **1992**, *150*, 243–269.
110. Manne, S.; Cleveland, J. P.; Gaub, H. E.; Stucky, G. D.; Hansma, P. K. *Langmuir* **1994**, *10*, 4409–4413.
111. Atkin, R.; Craig, V. S. J.; Wanless, E. J.; Biggs, S. *Advances in Colloid and Interface Science* **2003**, *103*, 219–304.
112. Hansma, H. G.; Gould, S. A. C.; Hansma, P. K.; Gaub, H. E.; Longo, M. L.; Zasadzinski, J. A. N. *Langmuir* **1991**, *7*, 1051–1054.
113. Ese, M.-H.; Sjöblom, J.; Djuve, J.; Pugh, R. *Colloid and Polymer Science* **2000**, *278*, 532–538.
114. Weisenhorn, A. L.; Drake, B.; Prater, C. B.; Gould, S. A. C.; Hansma, P. K.; Ohnesorge, F.; Egger, M.; Heyn, S. P.; Gaub, H. E. *Biophys. J.* **1990**, *58*, 1251–1258.
115. Hansma, H. G.; Sinsheimer, R. L.; Li, M. Q.; Hansma, P. K. *Nucleic Acids Res.* **1992**, *20*, 3585–3590.
116. Sato, H.; Ohtsu, T.; Komasawa, I. *Journal of Colloid and Interface Science* **2000**, *230*, 200–204.
117. Grabar, K. C.; Brown, K. R.; Keating, C. D.; Stranick, S. J.; Tang, S. L.; Natan, M. J. *Analytical Chemistry* **1997**, *69*, 471–477.
118. Wang, K.; Wu, J. S.; Zeng, H. M. *Composites Science and Technology* **2001**, *61*, 1529–1538.
119. Ray, S.; Bhowmick, A. K.; Bandyopadhyay, S. *Rubber Chemistry and Technology* **2003**, *76*, 1091–1105.
120. Denes, F. S.; Manolache, S. *Prog. Polym. Sci.* **2004**, *29*, 815–885.
121. Øye, G.; Roucoules, V.; Cameron, A. M.; Oates, L. J.; Cameron, N. R.; Steel, P. G.; Badyal, J. P. S.; Davis, B. G.; Coe, D.; Cox, R. A. *Langmuir* **2002**, *18*, 8996–8999.
122. Øye, G.; Roucoules, V.; Oates, L. J.; Cameron, A. M.; Cameron, N. R.; Steel, P. G.; Badyal, J. P. S.; Davis, B. G.; Coe, D. M.; Cox, R. A. *Journal of Physical Chemistry B* **2003**, *107*, 3496–3499.
123. Badyal, J. P.; Cameron, A. M.; Cameron, N. R.; Oates, L. J.; Øye, G.; Steel, P. G.; Davis, B. G.; Coe, D. M.; Cox, R. A. *Polymer* **2004**, *45*, 2185–2192.
124. Badyal, J. P.; Cameron, A. M.; Cameron, N. R.; Coe, D. M.; Cox, R.; Davis, B. G.; Oates, L. J.; Øye, G.; Spanos, C.; Steel, P. G. *Chemical Communications* **2004**, *12*, 1402–1403.
125. Kvande, I.; Øye, G.; Ochoa-Fernández, E.; Hammer, N.; Rønning, M.; Holmen, A.; Sjöblom, J.; Chen, D. *Nano Letters* (Submitted).
126. Good, R. J. *Journal of Adhesion Science and Technology* **1992**, *6(12)*, 1269–1302.
127. Neumann, A. W.; Good, R. J. *Surface and Colloid Science* **1979**, *11*, 31–91.
128. Hunter, R. J. *Introduction to Modern Colloid Science*; Oxford Science Publications: Oxford, 1993.
129. Barchini, R.; Saville, D. A. *Langmuir* **1996**, *12*, 1442–1445.
130. Neves, G. B. M.; Dos Anjos de Sousa, M.; Travalloni-Louvisse, A. M.; Lucas, E. F.; Gonzalez, G. *Petroleum Science and Technology* **2001**, *19*, 35–43.
131. Leon, O.; Rogel, E.; Torres, G.; Lucas, A. *Petroleum Science and Technology* **2000**, *18*, 913.
132. Berne, B. J.; Pecora, R. *Dynamic Light Scattering: With Applications to Chemistry, Biology and Physics*; Dover Publications: New York, 2000.
133. Van de Hulst, H. C. *Light Scattering by Small Particles*; Dover: New York, 1981.
134. Koppel, D. E. *Journal of Chemical Physics* **1972**, *57*, 4814.
135. Provencher, S. W. *Computer Physics Communications* **1982**, *27*, 213–227.
136. Provencher, S. W. *Computer Physics Communications* **1982**, *27*, 229–242.
137. Lawson, C. L.; Hanson, R. J. In *Solving Least Square Problems*; Prentice Hall: Englewood Cliffs, NJ, 1974.
138. Lawson, C. L.; Hanson, R. J. *Solving Least Squares Problems*; SIAM: Philadelphia, 1995.
139. Wagner, J.; Hartl, W.; Hempelmann, R. *Langmuir* **2000**, *16*, 4080–4085.
140. Sedlak, M. *Langmuir* **1999**, *15*, 4045–4051.

141. Dalgleish, D. G.; Hallett, F. R. *Food Research International* **1995**, *28*, 181–193.
142. Tkachenko, A. G.; Xie, H.; Coleman, D.; Glomm, W.; Ryan, J.; Anderson, M. F.; Franzen, S.; Feldheim, D. L. *Journal of the American Chemical Society* **2003**, *125*, 4700–4701.
143. De Smet, Y.; Deriemaeker, L.; Parloo, E.; Finsy, R. *Langmuir* **1999**, *15*, 2327–2332.
144. Holthoff, H.; Egelhaaf, S. U.; Borkovec, M.; Schurtenberger, P.; Sticher, H. *Langmuir* **1996**, *12*, 5541–5549.
145. Holthoff, H.; Borkovec, M.; Schurtenberger, P. *Physical Review E* **1997**, *56*, 6945–6953.
146. Holthoff, H.; Schmitt, A.; FernandezBarbero, A.; Borkovec, M.; CabrerizoVilchez, M. A.; Schurtenberger, P.; HidalgoAlvarez, R. *Journal of Colloid and Interface Science* **1997**, *192*, 463–470.
147. Wilcoxon, J. P.; Martin, J. E.; Schaefer, D. W. *Physical Review A* **1989**, *39*, 2675–2688.
148. Anisimov, M. A.; Yudin, I. K.; Nikitin, V.; Nikolaenko, G.; Chernoutsan, A.; Toulhoat, H.; Frot, D.; Briolant, Y. *Journal of Physical Chemistry* **1995**, *99*, 9576–9580.
149. Yudin, I. K.; Nikolaenko, G. L. *NATO ASI Series, Series 3: High Technology* **1997**, *40*, 341–352.
150. Yudin, I. K.; Nikolaenko, G. L.; Gorodetskii, E. E.; Kosov, V. I.; Melikyan, V. R.; Markhashov, E. L.; Frot, D.; Briolant, Y. *Journal of Petroleum Science & Engineering* **1998**, *20*, 297–301.
151. Yudin, I. K.; Nikolaenko, G. L.; Gorodetskii, E. E.; Markhashov, E. L.; Frot, D.; Briolant, Y.; Agayan, V. A.; Anisimov, M. A. *Petroleum Science and Technology* **1998**, *16*, 395–414.
152. McHale, J. L. *Molecular Spectroscopy*; 1st ed.; Prentice-Hall Inc.: Upper Saddle River, New Jersey, 1999.
153. Atkins, P. W. *Physical Chemistry*; 5th ed.; Oxford University Press: Oxford, 1994.
154. Brust, M.; Kiely, C. J. *Colloids and Surfaces a – Physicochemical and Engineering Aspects* **2002**, *202*, 175–186.
155. Kreibig, U.; Genzel, L. *Surface Science* **1985**, *156*, 678–700.
156. Franzen, S.; Folmer, J. C. W.; Glomm, W. R.; O'Neal, R. *Journal of Physical Chemistry A* **2002**, *106*, 6533–6540.
157. Xie, H.; Tkachenko, A. G.; Glomm, W. R.; Ryan, J. A.; Brennaman, M. K.; Papanikolas, J. M.; Franzen, S.; Feldheim, D. L. *Analytical Chemistry* **2003**, *75*, 5797–5805.
158. Chandrasekharan, N.; Kamat, P. V.; Hu, J. Q.; Jones, G. *Journal of Physical Chemistry B* **2000**, *104*, 11103–11109.
159. Dawson, A.; Kamat, P. V. *Journal of Physical Chemistry B* **2001**, *105*, 960–966.
160. Elghanian, R.; Storhoff, J. J.; Mucic, R. C.; Letsinger, R. L.; Mirkin, C. A. *Science* **1997**, *277*, 1078–1081.
161. Mirkin, C. A.; Letsinger, R. L.; Mucic, R. C.; Storhoff, J. J. *Nature* **1996**, *382*, 607–609.
162. Mirkin, C. A. *Inorganic Chemistry* **2000**, *39*, 2258–2272.
163. Mirkin, C. A. *Mrs Bulletin* **2000**, *25*, 43–54.
164. Reynolds, R. A.; Mirkin, C. A.; Letsinger, R. L. *Journal of the American Chemical Society* **2000**, *122*, 3795–3796.
165. Storhoff, J. J.; Elghanian, R.; Mucic, R. C.; Mirkin, C. A.; Letsinger, R. L. *Journal of the American Chemical Society* **1998**, *120*, 1959–1964.
166. Storhoff, J. J.; Mirkin, C. A. *Chemical Reviews* **1999**, *99*, 1849–1862.
167. Storhoff, J. J.; Lazarides, A. A.; Mucic, R. C.; Mirkin, C. A.; Letsinger, R. L.; Schatz, G. C. *Journal of the American Chemical Society* **2000**, *122*, 4640–4650.
168. Bronstein, L. M. In *Colloid Chemistry 1*; Springer-Verlag Berlin: Berlin, 2003; Vol. 226, pp 55–89.
169. Chen, W.; Cai, W. P.; Liang, C. H.; Zhang, L. D. *Materials Research Bulletin* **2001**, *36*, 335–342.
170. Chen, W.; Cai, W. P.; Zhang, L.; Wang, G. Z.; Zhang, L. D. *Journal of Colloid and Interface Science* **2001**, *238*, 291–295.
171. Chen, W.; Cai, W. P.; Wang, G. Z.; Zhang, L. *Applied Surface Science* **2001**, *174*, 51–54.
172. Chen, W.; Cai, W. P.; Zhang, Z. P.; Zhang, L. *Chemistry Letters* **2001**, 152–153.
173. Glomm, W. R.; Øye, G.; Walmsley, J.; Sjöblom, J. *Journal of Dispersion Science and Technology* **2005**, *26*, 729–744.
174. Alvarez, M. M.; Khoury, J. T.; Schaaff, T. G.; Shafigullin, M. N.; Vezmar, I.; Whetten, R. L. *Journal of Physical Chemistry B* **1997**, *101*, 3706–3712.

175. Cury, L. A.; Ladeira, L. O.; Righi, A. *Synthetic Metals* **2003**, *139*, 283–286.
176. Chumanov, G.; Sokolov, K.; Cotton, T. M. *Journal of Physical Chemistry* **1996**, *100*, 5166–5168.
177. Glomm, W. R.; Anthireya, S. J.; Brennaman, M. K.; Papanikolas, J. M.; Franzen, S. *J. Phys. Chem* (Submitted).
178. Lakowicz, J. R. *Principles of Fluorescence Spectroscopy*; Kluwer Academic/Plenum: New York, 1999.
179. Ford, G. W.; Weber, W. H. *Phys. Rep.* **1984**, *113*, 195–287.
180. Chance, R. R.; Prock, A.; Silbey, R. *Adv. Chem. Phys.* **1978**, *37*, 1–65.
181. Barnes, W. L. *J. Mod. Opt.* **1998**, *45*, 661–699.
182. Gersten, J. I.; Nitzan, A. *Surf. Sci.* **1985**, *158*, 165–189.
183. Kummerlen, J.; Leitner, A.; Brunner, H.; Aussenegg, F. R.; Wokaun, A. *Mol. Phys.* **1993**, *80*, 1031–1046.
184. Gersten, J. I.; Nitzan, A. *J. Chem. Phys.* **1981**, *75*, 1139–1152.
185. Gersten, J. I.; Nitzan, A. *Chem. Phys. Lett.* **1984**, *104*, 31–37.
186. Hua, X. M.; Gersten, J. I.; Nitzan, A. *J. Chem. Phys.* **1985**, *83*, 3650–3659.
187. Lakowicz, J. R. *Analytical Biochemistry* **2001**, *298*, 1–24.
188. Lakowicz, J. R.; Shen, Y.; D'Auria, S.; Malicka, J.; Fang, J.; Gryczynski, Z.; Gryczynski, I. *Analytical Biochemistry* **2002**, *301*, 261–277.
189. Strickler, S. J.; Berg, R. A. *J. Chem. Phys.* **1962**, *37*, 814–822.
190. Fleming, C. N.; Maxwell, K. A.; DeSimone, J. M.; Meyer, T. J.; Papanikolas, J. M. *Journal of the American Chemical Society* **2001**, *123*, 10336–10347.
191. Fleming, C. N.; Dupray, L. M.; Papanikolas, J. M.; Meyer, T. J. *Journal of Physical Chemistry A* **2002**, *106*, 2328–2334.
192. Brennaman, M. K.; Alstrum-Acevedo, J. H.; Fleming, C. N.; Jang, P.; Meyer, T. J.; Papanikolas, J. M. *Journal of the American Chemical Society* **2002**, *124*, 15094–15098.
193. Kleverlaan, C. J.; Indelli, M. T.; Bignozzi, C. A.; Pavanin, L.; Scandola, F.; Hasselman, G. M.; Meyer, G. J. *Journal of the American Chemical Society* **2000**, *122*, 2840–2849.
194. Bignozzi, C. A.; Schoonover, J. R.; Scandola, F. In *Molecular Level Artificial Photosynthetic Materials*; John Wiley & Sons Inc: New York, 1997; Vol. 44, pp 1–95.
195. Bignozzi, C. A.; Argazzi, R.; Kleverlaan, C. J. *Chemical Society Reviews* **2000**, *29*, 87–96.
196. Gust, D.; Moore, T. A.; Moore, A. L. *Accounts of Chemical Research* **2001**, *34*, 40–48.
197. Hissler, M.; McGarrah, J. E.; Connick, W. B.; Geiger, D. K.; Cummings, S. D.; Eisenberg, R. *Coordination Chemistry Reviews* **2000**, *208*, 115–137.
198. Slate, C. A.; Striplin, D. R.; Moss, J. A.; Chen, P. Y.; Erickson, B. W.; Meyer, T. J. *Journal of the American Chemical Society* **1998**, *120*, 4885–4886.
199. Tkachenko, A. G.; Xie, H.; Ryan, J.; Glomm, W. R.; Franzen, S.; Feldheim, D. L. In *Bionanotechnology Protocols*; Rosenthal, S., Wright, D., Eds.; Humana Press, Inc.: New York, **2005**, pp. 85–99.
200. Tkachenko, A. G.; Xie, H.; Liu, Y. L.; Coleman, D.; Ryan, J.; Glomm, W. R.; Shipton, M. K.; Franzen, S.; Feldheim, D. L. *Bioconjugate Chemistry* **2004**, *15*, 482–490.
201. Hiemenz, P. C.; Rajagopalan, R. *Principles of Colloid and Surface Chemistry*; 3rd ed.; Marcel Dekker, Inc: New York, 1997.